

Fractional Chern mosaic in supermoiré graphene

Yves H. Kwan,¹ Tixuan Tan,² and Trithep Devakul²

¹*Princeton Center for Theoretical Science, Princeton University, Princeton NJ 08544, USA*

²*Department of Physics, Stanford University, Stanford, CA 94305, USA*

We propose the realization of a fractional Chern mosaic: a state characterized by a spatially varying topological order. This state is enabled by a separation of length scales that emerges when three graphene sheets are sequentially rotated by a small twist angle. The resulting structure features not only conventional moiré lattices, but also a much larger supermoiré lattice. We demonstrate that a fractional Chern mosaic arises when electron correlations induce fractionalization locally on the moiré scale, while the pattern of fractionalization varies at the supermoiré scale.

I. INTRODUCTION

The importance of length scales in physics is exemplified in the rise of two-dimensional moiré materials. Twist engineered moiré lattices on the nanometer scale provide an ideal platform for experimentally realizing a remarkable variety of quantum phenomena [1–4], from superconductivity [5–13] to fractional Chern insulators [14–20]. This rich physics is enabled by a separation of length scales between the atomic and moiré lattices. At experimentally relevant scales, the physics is governed by that of the moiré lattice, which behaves as a new artificial crystal.

The interplay of length scales is at the forefront in an emerging class of moiré materials with multiple incommensurate moiré lattices. Prominent examples are various multilayer graphene-hBN heterostructures [21–31] and twisted trilayer graphene at small, generic, twist angles [32–53]. The presence of two incommensurate moiré lattices introduces an additional large supermoiré (or “moiré-of-moiré”) length scale, which can be parametrically larger than the moiré lattices. This new supermoiré scale leads to another separation of length and energy scales, opening the door to especially intriguing correlated electronic states.

One especially striking example is the Chern mosaic [54–59]. In this state, electrons form Chern insulators at the moiré scale, but the Chern number varies across the supermoiré scale. The result is a mosaic of Chern insulators embedded in a network of topological domain walls. Here, we consider an even more exotic possibility: a “fractional Chern mosaic”, where electrons spontaneously fractionalize within local regions of fractional Chern insulators (FCI) [60–66], but with the pattern of fractionalization varying at the supermoiré scale. Such a fractional Chern mosaic would represent a novel class of quantum states characterized by a spatially varying topological order.

We propose the realization of a fractional Chern mosaic. Specifically, we focus on helical trilayer graphene (HTG), a prototypical supermoiré material consisting of three graphene sheets sequentially rotated by a small twist angle θ , i.e. in the configuration $(\theta_1, \theta_2, \theta_3) = (\theta, 0, -\theta)$. In HTG, adjacent layer pairs produce moiré lattices with periods $a_m \approx a_0/\theta$, which combine to form a

large supermoiré lattice with period $a_{sm} \approx a_0/\theta^2$, where $a_0 = 0.246\text{nm}$ is the graphene lattice constant. This supermoiré lattice, on the scale of a few hundred nanometers, was recently imaged with a scanning single-electron transistor (SET) [67]. Lattice relaxation creates large triangular moiré-periodic domains, referred to as h-HTG and \bar{h} -HTG, as illustrated in Fig. 1 [36, 37]. Due to the separation of lengthscales $a_{sm} \gg a_m$, it suffices to model the system as locally periodic within each domain. Within these periodic domains, the local moiré band structure gives rise to topological flat bands with valley-contrasting Chern number and opposing topology in adjacent domains [36–38]. Flat band ferromagnetism then leads to spontaneous time reversal symmetry breaking, as observed near a magic angle $\theta \approx 1.8^\circ$ [51]. The combined presence of broken time-reversal symmetry, flat Chern bands, and supermoiré periodicity sets the stage for the fractional Chern mosaic.

The task is to establish whether electrons within each domain can fractionalize. To achieve this, we perform a comprehensive analysis of the correlated physics at partial filling of the flat Chern bands. We begin by characterizing an additional momentum-dependent tunneling (MDT) term in the Hamiltonian, which originates from the decay of the interlayer tunneling amplitude as a function of the in-plane distance between the atomic p_z orbitals [68]. We find that accounting for MDT not only explains the particle-hole asymmetry observed in transport [51] but, crucially, stabilizes an FCI at filling factor $\nu = 3 + 1/3$. The predicted state, illustrated in Fig. 1a, features electron fractionalization into charge $e/3$ quasiparticles in a spatially varying way due to the opposing band topology in the h-HTG and \bar{h} -HTG domains, and can be experimentally unveiled by local scanning probes.

Non-interacting model—Our starting point is a generalized Bistritzer-MacDonald [69] continuum model description of the local band structure within each h-HTG (or \bar{h} -HTG) domain [36]. The K valley of h-HTG is described by

$$H_K = \begin{bmatrix} -iv\boldsymbol{\sigma} \cdot \nabla & T(\mathbf{r} - \mathbf{d}_t) & 0 \\ T^\dagger(\mathbf{r} - \mathbf{d}_t) & -iv\boldsymbol{\sigma} \cdot \nabla & T(\mathbf{r} - \mathbf{d}_b) \\ 0 & T^\dagger(\mathbf{r} - \mathbf{d}_b) & -iv\boldsymbol{\sigma} \cdot \nabla \end{bmatrix} \quad (1)$$

where $\boldsymbol{\sigma} = (\sigma_x, \sigma_y)$ acts on the microscopic sublattice, and $v = 8.8 \times 10^5 \text{ms}^{-1}$.

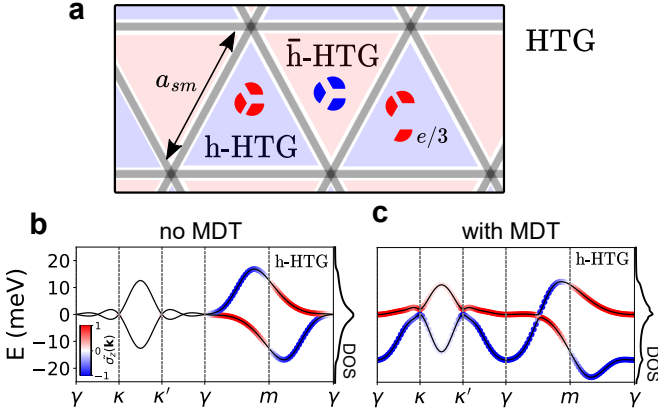


FIG. 1. **a)** Helical trilayer (HTG) relaxes on the supermoiré scale a_{sm} into h-HTG and \bar{h} -HTG domains that are locally moiré-periodic, and separated by gapless domain walls (grey). Fractionalization within the domains generates a fractional Chern mosaic. **b)** Band structure in valley K of the h-HTG domain in the absence of momentum-dependent tunneling (MDT). The central two bands are colored according to Chern-sublattice polarization $\tilde{\sigma}_z(\mathbf{k})$, where red (blue) indicates polarization onto the A (B) sublattice. Right line trace plots the density of states. **c)** Same as **b)** except in the presence of MDT.

In the absence of MDT, the interlayer tunneling is

$$T(\mathbf{r}) = \begin{bmatrix} w_{AA}t_0(\mathbf{r}) & w_{AB}t_{-1}(\mathbf{r}) \\ w_{AB}t_1(\mathbf{r}) & w_{AA}t_0(\mathbf{r}) \end{bmatrix}$$

$$t_\alpha(\mathbf{r}) = \sum_{n=0}^2 e^{\frac{2\pi i}{3}n\alpha} e^{i\mathbf{q}_n \cdot \mathbf{r}} \quad (2)$$

$$q_{n,x} + iq_{n,y} = -ik_\theta e^{\frac{2\pi i}{3}n},$$

where $k_\theta = 2K_D \sin \frac{\theta}{2}$, with $K_D = \frac{4\pi}{3a_0}$ the Dirac wavevector, and we fix $(w_{AA}, w_{AB}) = (75 \text{ meV}, 110 \text{ meV})$. Within the h-HTG domain, the relative interlayer moiré shift is $\mathbf{d}_t - \mathbf{d}_b = \frac{1}{3}(\mathbf{a}_2 - \mathbf{a}_1)$, where $\mathbf{a}_{1,2} = \frac{4\pi}{3k_\theta}(\pm \frac{\sqrt{3}}{2}, \frac{1}{2})$ are the basis moiré vectors. We focus only on the physics within an h-HTG domain, as the \bar{h} -HTG domains are related by \hat{C}_{2z} symmetry.

Eq. 1 and 2 obey an exact particle-hole-inversion symmetry¹ (PHS) that is strongly broken in experiment [51], where correlated states appear only for electron doping. This symmetry is broken by considering the finite range of interlayer hopping, which generates MDT. This is incorporated to leading order by making the replacement

$$t_\alpha(\mathbf{r}) \rightarrow \sum_{n=0}^2 e^{\frac{2\pi i}{3}n\alpha} e^{i\mathbf{q}_n \cdot \mathbf{r}} (1 + \lambda_{\text{MDT}} \hat{\mathbf{q}}_{n,\perp} \cdot \vec{\nabla}), \quad (3)$$

where $\hat{\mathbf{q}}_{n,\perp} = [\cos(\frac{2\pi}{3}n), \sin(\frac{2\pi}{3}n)]$ is a unit vector perpendicular to \mathbf{q}_n . We take a realistic $\lambda_{\text{MDT}} \approx -2.3 \text{ \AA}$, as

derived in App. A.

Fig. 1b,c shows the non-interacting band structure of $\theta = 1.8^\circ$ h-HTG within a single spin-valley sector. Regardless of MDT, we obtain a pair of narrow bands separated by large gaps $\gtrsim 80 \text{ meV}$ to higher remote bands that are not shown. The non-trivial topology is unveiled by diagonalizing the sublattice operator σ_z projected to the central bands [70–72]. This yields the so-called Chern basis indexed by a ‘Chern-sublattice’ label $\tilde{\sigma} = A, B$ according to the dominant sublattice polarization². Within valley K , these bands have Chern numbers

$$C_{K,A} = 1, \quad C_{K,B} = -2, \quad (4)$$

and the corresponding values for valley \bar{K} and the \bar{h} -HTG domain can be obtained by time-reversal and \hat{C}_{2z} . The blue and red colors indicate the expectation value of $\langle \tilde{\sigma}_z \rangle \equiv \langle P_A \rangle - \langle P_B \rangle$, where P_σ is the projector onto the $\tilde{\sigma}$ band.

In the absence of MDT (Fig. 1b), the central bands obey PHS as reflected in the density of states. Band eigenstates with predominantly B character ($\langle \tilde{\sigma}_z \rangle \approx -1$) are more dispersive than those with A character, but both have the same energy when averaged over the mBZ. To make this concrete, we can rotate to the Chern basis and switch off the off-diagonal hybridization to define the dispersions $E_{\tilde{\sigma}_z}(\mathbf{k})$ (see App. B). At $\theta = 1.8^\circ$, we find that $E_A(\mathbf{k})$ and $E_B(\mathbf{k})$ have zero average, but bandwidths 7.2 meV and 30.4 meV respectively.

In contrast, introduction of MDT (Fig. 1c) lowers the energy of the B basis relative to the A basis. At $\theta = 1.8^\circ$, $E_A(\mathbf{k})$ has a mean energy of 1.0 meV and is bounded by -2.9 meV and 4.2 meV , while $E_B(\mathbf{k})$ has a mean energy of -6.4 meV and is bounded by -22.4 meV and 9.4 meV . This strongly breaks the PHS, as evidenced by the substantial asymmetry of the density of states. These details will become important soon when considering correlated states.

Interactions—We consider gate-screened Coulomb interactions $V(q) = \frac{e^2}{2\epsilon_0\epsilon_r q} \tanh qd_{sc}$, where the gate distance is $d_{sc} = 25 \text{ nm}$ and the relative permittivity $\epsilon_r \simeq 8 - 15$ is left as a tuning parameter. The large single-particle remote gaps permit projection onto the two central bands per spin and valley

$$H_{\text{int}} = \frac{1}{2A} \sum_{\mathbf{q}} V(q) \delta \hat{\rho}_{\mathbf{q}} \delta \hat{\rho}_{-\mathbf{q}} \quad (5)$$

where A is the system area, and $\delta \hat{\rho}_{\mathbf{q}} = \hat{\rho}_{\mathbf{q}} - 4\bar{\rho}_{\mathbf{q}}$ is the projected density operator measured relative to the mean density $\bar{\rho}_{\mathbf{q}}$ of the central bands (this is the so-called ‘average’ interaction scheme) [52]. H_{int} satisfies a $U(2)_K \times U(2)_{\bar{K}}$ flavor symmetry, which includes

¹ This is only weakly broken when introducing the small twists in the Pauli terms.

² $\tilde{\sigma}$ refers to the Chern basis, while σ indexes the microscopic sublattice. They become equivalent in the chiral limit. We will often use the terms Chern and sublattice interchangeably.

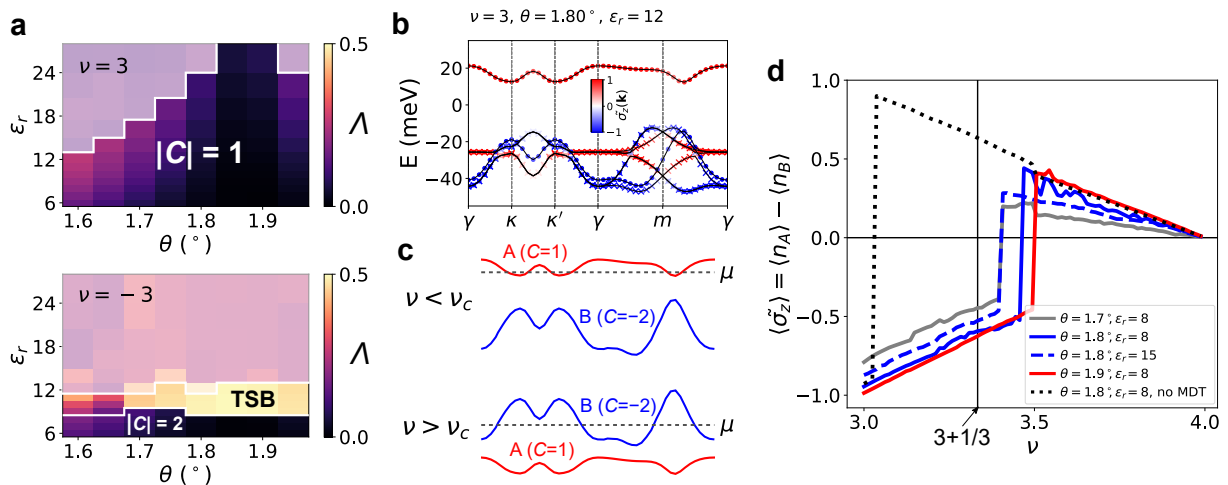


FIG. 2. **a)** HF phase diagram as a function of twist angle θ and relative permittivity ϵ_r at $\nu = +3$ (top) and $\nu = -3$ (bottom). White shaded regions indicate gapless states. Λ , defined in the main text, is a measure of how far the HF solution is from an idealized strong-coupling state. TSB indicates various states that break moiré translation symmetry. System size is 12×12 , and we allow for spontaneous doubling or tripling of the moiré unit cell along both directions. **b)** HF band structure of the $\nu = +3$ Chern insulator. The bands are colored according to their Chern-sublattice polarization. Dots (crosses) denote spin up (down). System size is 24×24 . **c)** Schematic of Chern-sublattice transitions induced by the sublattice asymmetry in the effective dispersion. **d)** HF calculations of Chern-sublattice polarization $\langle \tilde{\sigma}_z \rangle$ for fillings $3 \leq \nu \leq 4$. $\langle \tilde{\sigma}_z \rangle$ is defined as the difference of the occupation numbers of the A and B Chern-sublattice bands per moiré unit cell. We enforce moiré translation symmetry and valley $U_v(1)$ symmetry. Calculations are performed with MDT unless otherwise indicated. System size is 18×18 .

charge- $U(1)_c$ and valley- $U(1)_v$ conservation, and valley-dependent $SU(2)_s$ spin-rotations.

Hartree-Fock phase diagram— We first consider the physics at integer fillings within Hartree-Fock (HF) theory. In the absence of MDT, Ref. [52] identified a hierarchy of so-called “strong-coupling” insulators at integer fillings ν . These phases can be understood by fully polarizing into $\nu + 4$ of the eight total Chern bands indexed by spin $s \in \{\uparrow, \downarrow\}$, valley $\tau \in \{K, K'\}$, and Chern-sublattice $\tilde{\sigma}_z \in \{A, B\}$, with the associated Chern number following from Eq. 4. The phase diagram in Ref. [52] was identical under $\nu \leftrightarrow -\nu$ due to PHS.

In contrast, MDT leads to qualitatively different behaviors at negative and positive integer fillings in our HF calculations (Fig. 2a). We diagnose the strong-coupling nature by the deviation from full $(\tau, s, \tilde{\sigma})$ -polarization

$$\Lambda \equiv \max_{\tau, s, \tilde{\sigma}} \left[\min(\langle n_{\tau, s, \tilde{\sigma}} \rangle, 1 - \langle n_{\tau, s, \tilde{\sigma}} \rangle) \right], \quad (6)$$

where $\langle n_{\tau, s, \tilde{\sigma}} \rangle$ is the mBZ-averaged occupation number for the Chern band $\tilde{\sigma}$ in valley τ and spin s . Λ vanishes for an idealized strong-coupling insulator, while it can take values as large as 0.5 for generic states. For $\nu = +3$, we find a strong-coupling $|C| = 1$ insulator for a range of θ , including for very weak interactions $\epsilon_r \gtrsim 25$. On the other hand for $\nu = -3$, the strong-coupling phase only exists for relatively strong interactions $\epsilon_r \lesssim 9$. Lowering the interaction strength leads to gapless states, or various gapped phases with intervalley coherence and translation symmetry-breaking [52, 73]. Analogous results hold for other integer fillings (Fig. S4), demonstrat-

ing that MDT can explain the pronounced particle-hole asymmetry observed in transport [51].

Fig. 2b shows the HF band structure of the $|C| = 1$ insulator at $\nu = +3$. The state is fully spin-valley polarized within the flat-band manifold, and the strong-coupling nature is evidenced by the near total $\tilde{\sigma}_z$ polarization of the conduction band. In the partially-filled flavor, the system occupies the B band (blue) with lower mean kinetic energy, leaving a narrow unfilled A band (red) with $|C| = 1$.

Sublattice transitions—At $\nu = 3$, the unfilled conduction band is a narrow $|C| = 1$ band of predominantly $\tilde{\sigma} = A$ character, with favorable quantum geometry (Fig. S5) for hosting FCIs when fractionally occupied. For this to occur, it is crucial that the notion of an isolated conduction A band remains valid at higher fractional fillings like $\nu = 3 + \frac{1}{3}$.

To this end, we discover a cascade of sublattice transitions (Fig. 2c,d), whose mechanism relies on two key ingredients: (i) sublattice ferromagnetism induced by the dominant Coulomb interactions, and (ii) the lower average but higher peak kinetic energy of the B band compared to the A band. In the following, we discuss the cascade for the filling range $3 \leq \nu \leq 4$ assuming full flavor polarization (i.e. flat bands in three of four spin-valley flavors are fully filled). Exactly at $\nu = 3$, occupying either Chern band of the remaining flavor yields a valid exchange-driven strong-coupling insulator, but the system chooses to form the $|C| = 1$ insulator and fill the B band due to its lower average kinetic energy, yielding a $\langle \tilde{\sigma}_z \rangle \approx -1$ state. As electrons are doped into the sys-

tem, they naturally populate the empty A band (Fig. 2c, top), which gradually degrades the initial negative sublattice polarization $-1 < \langle \tilde{\sigma}_z \rangle < 0$. Eventually we reach a critical filling ν_c where the system energetically prefers to instead fully occupy the A band and partially occupy the B band so that $\langle \tilde{\sigma}_z \rangle > 0$ (Fig. 2c, bottom). The reason is that doing so allows the system to empty the parts of the B band that are kinetically costly, while respecting the tendency towards sublattice polarization. ν_c is determined by the interplay between the relative energy gain from fully polarizing the B band over the A band, and the kinetic cost of occupying the high energy parts of the B band. The outcome is an abrupt sign change of the sublattice polarization at ν_c .

Fig. 2d tracks the self-consistent HF sublattice polarization. For all parameters, $\langle \tilde{\sigma}_z \rangle$ starts off near -1 and increases linearly with a gradient close to 1 as the empty A band is progressively occupied. With MDT, we find a strongly first-order sublattice jump at which $\langle \tilde{\sigma}_z \rangle$ changes sign. Crucially, the transition filling $\nu_c \approx 3.5$ is greater than $3 + \frac{1}{3}$ for realistic parameters. The enhanced dispersion of the B band means that the Fermi surfaces for $\nu > \nu_c$ are often flavor-degenerate, but the phase for $\nu < \nu_c$ is always fully flavor polarized. These findings are consistent with the experimental observation of AHE persisting to $\nu \approx 3.5$ [51]. ν_c is lowered when increasing ϵ_r . If MDT is neglected (dotted lines), the sublattice transition occurs almost immediately upon electron doping $\nu = +3$. The reason is that without MDT, the average kinetic energies of the A and B bands are identical (Fig. 2a), and only the sublattice exchange anisotropy of $\lesssim 0.5$ meV favors occupying the B band at $\nu = +3$ [52]. This tiny splitting is easily swamped at small ν_c by the kinetically-driven mechanism explained above, underscoring the importance of MDT in faithfully capturing the sublattice physics. Similar sublattice transitions occur between every non-negative integer filling, but none occur for $\nu < 0$, where there is significantly less symmetry-breaking (Fig. S7).

Exact diagonalization—We use exact diagonalization (ED) to investigate whether FCIs can be stabilized at fractional fillings. Since full calculations in the eight central bands are expensive, it is necessary to truncate the ‘active’ part of the many-body Hilbert space. In Fig. 3a, we first present 1-band ED results at $\nu = 3 + \frac{1}{3}$, where the active subspace is restricted to the $|C| = 1$ conduction band of the $\nu = +3$ HF insulator. In other words, we constrain the other seven HF bands to be fully occupied³, and work at $1/3$ filling of the remaining Chern band which is spin-valley polarized and of predominantly $\tilde{\sigma} = A$ character (see Fig. 2b). We obtain an FCI for $\epsilon_r = 8, 15$ on a system with $N = 30$ unit cells, as evident from the three-fold quasi-degenerate ground states with

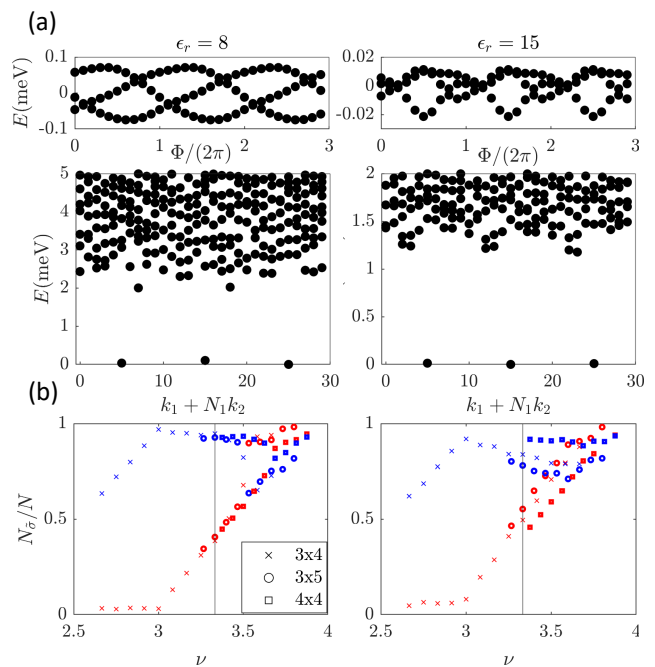


FIG. 3. **a)** 1-band ED calculation on the 5×6 cluster at $\nu = 3 + 1/3$. Bottom row shows the momentum-resolved many-body spectrum for $\epsilon_r = 8$ and 15 . Top row shows the corresponding evolutions of the three quasi-degenerate ground states under flux threading Φ . **b)** 2-band ED calculation of the Chern-sublattice polarization as a function of filling. Different symbols (see legend) refer to various lattice geometries with corresponding system sizes $N = 12, 15, 16$. $N_{\tilde{\sigma}}$ is the expectation value of the particle occupation in the Chern-sublattice basis. Red (blue) corresponds to the A (B) basis. The vertical line indicates $\nu = 3 + 1/3$. All calculations are performed at $\theta = 1.8^\circ$ and with MDT.

correct momenta that remain gapped under flux threading. In App. D, we show $N = 27$ results that rule out charge density waves.

Next, we perform ED calculations where we only constrain that three flavors are fully occupied, leading to the restriction $2 \leq \nu \leq 4$. We emphasize that this effective 2-band calculation is *exact* within the maximally spin-valley-polarized symmetry sector of the eight central bands. From the HF results, we anticipate that the ground state indeed lies in this flavor sector from $\nu = +3$ up to at least the sublattice transition at ν_c (see App. C 4). Importantly, this 2-band calculation faithfully captures the interplay between the $\tilde{\sigma} = A, B$ bands.

Fig. 3b plots the Chern-sublattice densities $\langle n_A \rangle$ and $\langle n_B \rangle$ in the 2-band calculation as a function of ν . Owing to the increased computational difficulty, we collate results for several system sizes. Consistent with the HF analysis, the $\nu = +3$ ground state is strongly polarized into the B band and is essentially a gapped single Slater determinant (see App. D). Upon electron-doping for $\epsilon_r = 8$, the B band maintains a large occupancy $> 90\%$ such that the additional carriers primarily pop-

³ We therefore include the Hartree and Fock potentials from these non-active bands.

ulate the A band. Crucially, this picture still holds at $\nu = 3 + \frac{1}{3}$ across multiple lattice geometries, lending credence to the 1-band ED. The theory of sublattice transitions is corroborated by the abrupt jump at $\nu_c \approx 3.5$. For $\epsilon_r = 15$, the B band depopulates more appreciably for certain system sizes when adding electrons to the $\nu = +3$ insulator, though we still find kinks in the sublattice occupations around $\nu_c \approx 3.5$. We note that direct signatures of FCIs in our multi-band calculations are present but not fully robust (see App. D4), likely due to finite-size effects since the largest size⁴ for which we have 2-band data at $\nu = 3 + \frac{1}{3}$ is smaller than the threshold N beyond which 1-band ED robustly yields FCIs.

Fractional Chern mosaics — Having found evidence for FCIs within the h-HTG domains, we now zoom out and re-examine the structure of HTG at $\nu = 3 + 1/3$ as a whole. In the h-HTG domain, electrons within the A band of a particular spin-valley (τ, s) flavor fractionalizes. The resulting state has a local Hall conductivity $\sigma_{xy} = -\frac{2}{3}\tau_z \frac{e^2}{h}$ where $\tau_z = 1$ (for K) or -1 (for K'). The fractional Hall conductivity can be decomposed as $-\frac{2}{3} = -1 + \frac{1}{3}$, where -1 arises from the Chern insulator at $\nu = 3$, and $1/3$ from the FCI. Since the local physics in the \bar{h} -HTG domain is related by \hat{C}_{2z} , the corresponding FCI there will arise from a partially filled B band with local $\sigma_{xy} = \frac{2}{3}\tau_z \frac{e^2}{h}$. Since the spin-valley polarization is determined spontaneously, there are multiple qualitatively distinct fractional Chern mosaics that may occur. Which of these scenarios is favored will likely depend on fine details of the domain wall energetics [52, 58].

Consider the case where the valley polarizations in the h-HTG and \bar{h} -HTG domains are identical. In this case, a mosaic of local $\sigma_{xy} = \pm \frac{2}{3} \frac{e^2}{h}$ domains is formed. The domain walls necessarily host fractionally charged topological chiral edge modes. In both types of domains, electrons fractionalize into charge $e/3$ quasiparticles as is known for the $1/3$ Laughlin state. However, the anyonic exchange phase $e^{\pm i\frac{\pi}{3}}$ will be opposite for quasiparticles in the two types of domains. The result is a novel state in which fractionally charged quasiparticles exhibit spatially varying anyonic statistics.

Another possibility is that the valley polarizations will be opposite in the two domains. This configuration will be favored by a small external magnetic field. For concreteness, suppose that the FCI arises in the K valley for h-HTG, and in the K' valley for \bar{h} -HTG. In this case, while both domains have local $\sigma_{xy} = -\frac{2}{3} \frac{e^2}{h}$, we consider this state a fractional Chern mosaic since the fractionally charged $e/3$ quasiparticles carry opposite valley quantum numbers in the two domains.

Discussion—Our results have important implications for recent and future experiments. The transport study

of Ref. [51] observed correlated features only for positive fillings in multiple magic-angle ($\theta \approx 1.7^\circ - 1.8^\circ$) HTG devices, consistent with our HF calculations in the presence of MDT. The anomalous Hall effect and density-tuned hysteresis observed near $3 \lesssim \nu \lesssim 3.5$ are consistent with the sublattice transition identified here via the kinetic mechanism at $\nu_c \approx 3.5$. Combined with the recent observation of supermoiré domains in (non magic-angle) HTG by Ref. [67], our analysis implies that a fractional Chern mosaic can be realized at $\nu = 3 + 1/3$, but is not likely visible in transport [51] due to the network of conducting domain walls and sample inhomogeneity. Local probes are ideal for resolving the real-space mosaic and detecting the local topological state. Scanning single-electron transistors (SET) [67, 74–76] can identify the state as an incompressible feature that disperses with perpendicular magnetic field B according to the Streda formula. Scanning tunneling microscopy (STM) [77–84] would further be able to directly image the cascade of sublattice transitions predicted in this work. We also note that the global \hat{C}_{2z} symmetry of pristine HTG implies that identical physics would be present in the h-HTG and \bar{h} -HTG domains, but alignment to the hBN substrate could introduce a sublattice splitting that favors fractionalization in only one type of domain.

Finally, while we have mainly focused on $\nu = 3 + \frac{1}{3}$, FCIs may exist at other fillings, especially those which are compatible with the picture above. The simplest candidates are Jain states at $\nu = 3 + \frac{k}{2k+1}$ for which $\nu < \nu_c$. The periodic resets in flavor and sublattice physics suggest that fractionalization could also occur around other integer fillings, a possibility which we leave for future theoretical studies.

In summary, we have predicted the realization of a fractional Chern mosaic enabled by a combination of local topological flat bands and supermoiré periodicity. Our results present an opportunity to engineer and explore novel intricate quantum states with spatially varying topological order.

ACKNOWLEDGMENTS

We thank Liqiao Xia, Aviram Uri, Ben Feldman, Sergio de la Barrera, Aaron Sharpe, and Jonah Herzog-Arbeitman for valuable discussions and comments. TD thanks Junkai Dong, Daniel Parker, Patrick Ledwith, Tomohiro Soejima, Ashvin Vishwanath, and Michael Zaletel for early contributions and discussions that inspired this project. TD and TT are supported by a startup fund at Stanford University. Some of the ED calculations were performed using the DiagHam software package.

⁴ The Hilbert space dimension per momentum at $N = 18, 21$ is

approximately 7×10^7 and 3×10^9 respectively.

- [1] E. Y. Andrei, D. K. Efetov, P. Jarillo-Herrero, A. H. MacDonald, K. F. Mak, T. Senthil, E. Tutuc, A. Yazdani, and A. F. Young, The marvels of moiré materials, *Nature Reviews Materials* **6**, 201 (2021).
- [2] K. F. Mak and J. Shan, Semiconductor moiré materials, *Nature Nanotechnology* **17**, 686 (2022).
- [3] D. M. Kennes, M. Claassen, L. Xian, A. Georges, A. J. Millis, J. Hone, C. R. Dean, D. Basov, A. N. Pasupathy, and A. Rubio, Moiré heterostructures as a condensed-matter quantum simulator, *Nature Physics* **17**, 155 (2021).
- [4] N. P. Wilson, W. Yao, J. Shan, and X. Xu, Excitons and emergent quantum phenomena in stacked 2d semiconductors, *Nature* **599**, 383 (2021).
- [5] Y. Cao, V. Fatemi, S. Fang, K. Watanabe, T. Taniguchi, E. Kaxiras, and P. Jarillo-Herrero, Unconventional superconductivity in magic-angle graphene superlattices, *Nature* **556**, 43 (2018).
- [6] M. Yankowitz, S. Chen, H. Polshyn, Y. Zhang, K. Watanabe, T. Taniguchi, D. Graf, A. F. Young, and C. R. Dean, Tuning superconductivity in twisted bilayer graphene, *Science* **363**, 1059 (2019).
- [7] X. Lu, P. Stepanov, W. Yang, M. Xie, M. A. Aamir, I. Das, C. Urgell, K. Watanabe, T. Taniguchi, G. Zhang, *et al.*, Superconductors, orbital magnets and correlated states in magic-angle bilayer graphene, *Nature* **574**, 653 (2019).
- [8] G. Chen, A. L. Sharpe, P. Gallagher, I. T. Rosen, E. J. Fox, L. Jiang, B. Lyu, H. Li, K. Watanabe, T. Taniguchi, *et al.*, Signatures of tunable superconductivity in a trilayer graphene moiré superlattice, *Nature* **572**, 215 (2019).
- [9] H. S. Arora, R. Polski, Y. Zhang, A. Thomson, Y. Choi, H. Kim, Z. Lin, I. Z. Wilson, X. Xu, J.-H. Chu, *et al.*, Superconductivity in metallic twisted bilayer graphene stabilized by wse2, *Nature* **583**, 379 (2020).
- [10] J. M. Park, Y. Cao, K. Watanabe, T. Taniguchi, and P. Jarillo-Herrero, Tunable strongly coupled superconductivity in magic-angle twisted trilayer graphene, *Nature* **590**, 249 (2021).
- [11] Z. Hao, A. Zimmerman, P. Ledwith, E. Khalaf, D. H. Najafabadi, K. Watanabe, T. Taniguchi, A. Vishwanath, and P. Kim, Electric field-tunable superconductivity in alternating-twist magic-angle trilayer graphene, *Science* **371**, 1133 (2021).
- [12] Y. Xia, Z. Han, K. Watanabe, T. Taniguchi, J. Shan, and K. F. Mak, Unconventional superconductivity in twisted bilayer wse2 (2024), arXiv:2405.14784 [cond-mat.mes-hall].
- [13] Y. Guo, J. Pack, J. Swann, L. Holtzman, M. Cothrine, K. Watanabe, T. Taniguchi, D. Mandrus, K. Barmak, J. Hone, A. J. Millis, A. N. Pasupathy, and C. R. Dean, Superconductivity in twisted bilayer wse2 (2024), arXiv:2406.03418 [cond-mat.mes-hall].
- [14] E. M. Spanton, A. A. Zibrov, H. Zhou, T. Taniguchi, K. Watanabe, M. P. Zaletel, and A. F. Young, Observation of fractional chern insulators in a van der waals heterostructure, *Science* **360**, 62 (2018).
- [15] Y. Xie, A. T. Pierce, J. M. Park, D. E. Parker, E. Khalaf, P. Ledwith, Y. Cao, S. H. Lee, S. Chen, P. R. Forrester, K. Watanabe, T. Taniguchi, A. Vishwanath, P. Jarillo-Herrero, and A. Yacoby, Fractional chern insulators in magic-angle twisted bilayer graphene, *Nature* **600**, 439–443 (2021).
- [16] J. Cai, E. Anderson, C. Wang, X. Zhang, X. Liu, W. Holtzmann, Y. Zhang, F. Fan, T. Taniguchi, K. Watanabe, *et al.*, Signatures of fractional quantum anomalous hall states in twisted mote2 bilayer, arXiv preprint arXiv:2304.08470 (2023).
- [17] Y. Zeng, Z. Xia, K. Kang, J. Zhu, P. Knüppel, C. Vaswani, K. Watanabe, T. Taniguchi, K. F. Mak, and J. Shan, Thermodynamic evidence of fractional chern insulator in moiré mote2, *Nature* **622**, 69 (2023).
- [18] F. Xu, Z. Sun, T. Jia, C. Liu, C. Xu, C. Li, Y. Gu, K. Watanabe, T. Taniguchi, B. Tong, J. Jia, Z. Shi, S. Jiang, Y. Zhang, X. Liu, and T. Li, Observation of integer and fractional quantum anomalous hall effects in twisted bilayer mote2, *Phys. Rev. X* **13**, 031037 (2023).
- [19] H. Park, J. Cai, E. Anderson, Y. Zhang, J. Zhu, X. Liu, C. Wang, W. Holtzmann, C. Hu, Z. Liu, *et al.*, Observation of fractionally quantized anomalous hall effect, *Nature* **622**, 74 (2023).
- [20] Z. Lu, T. Han, Y. Yao, A. P. Reddy, J. Yang, J. Seo, K. Watanabe, T. Taniguchi, L. Fu, and L. Ju, Fractional quantum anomalous hall effect in multilayer graphene, *Nature* **626**, 759 (2024).
- [21] X. Lai, D. Guerci, G. Li, K. Watanabe, T. Taniguchi, J. Wilson, J. H. Pixley, and E. Y. Andrei, Imaging self-aligned moiré crystals and quasicrystals in magic-angle bilayer graphene on hbn heterostructures, arXiv preprint arXiv:2311.07819 (2023).
- [22] Z. Wang, Y. B. Wang, J. Yin, E. Tóvári, Y. Yang, L. Lin, M. Holwill, J. Birkbeck, D. J. Perello, S. Xu, J. Zultak, R. V. Gorbachev, A. V. Kretinin, T. Taniguchi, K. Watanabe, S. V. Morozov, M. Anđelković, S. P. Milovanović, L. Covaci, F. M. Peeters, A. Mishchenko, A. K. Geim, K. S. Novoselov, V. I. Fal’ko, A. Knothe, and C. R. Woods, Composite super-moiré lattices in double-aligned graphene heterostructures, *Science Advances* **5**, 10.1126/sciadv.aay8897 (2019).
- [23] L. Wang, S. Zihlmann, M.-H. Liu, P. Makk, K. Watanabe, T. Taniguchi, A. Baumgartner, and C. Schonenberger, New generation of moiré superlattices in doubly aligned hbn/graphene/hbn heterostructures, *Nano letters* **19**, 2371 (2019).
- [24] N. R. Finney, M. Yankowitz, L. Muraleetharan, K. Watanabe, T. Taniguchi, C. R. Dean, and J. Hone, Tunable crystal symmetry in graphene–boron nitride heterostructures with coexisting moiré superlattices, *Nature nanotechnology* **14**, 1029 (2019).
- [25] M. M. Al Ezzi, J. Hu, A. Ariando, F. Guinea, and S. Adam, Topological flat bands in graphene super-moiré lattices, *Physical Review Letters* **132**, 126401 (2024).
- [26] D. Mao and T. Senthil, Quasiperiodicity, band topology, and moiré graphene, *Physical Review B* **103**, 115110 (2021).
- [27] N. Leconte and J. Jung, Commensurate and incommensurate double moiré interference in graphene encapsulated by hexagonal boron nitride, *2D Materials* **7**, 031005 (2020).
- [28] M. Andjelkovic, S. P. Milovanovic, L. Covaci, and F. M. Peeters, Double moiré with a twist: supermoiré in encap-

- sulated graphene, *Nano letters* **20**, 979 (2020).
- [29] J. Shi, J. Zhu, and A. MacDonald, Moiré commensurability and the quantum anomalous hall effect in twisted bilayer graphene on hexagonal boron nitride, *Physical Review B* **103**, 075122 (2021).
- [30] S. Grover, M. Bocarsly, A. Uri, P. Stepanov, G. Di Battista, I. Roy, J. Xiao, A. Y. Meltzer, Y. Myasoedov, K. Pareek, *et al.*, Chern mosaic and berry-curvature magnetism in magic-angle graphene, *Nature physics* **18**, 885 (2022).
- [31] A. Rothstein, C. Schattauer, R. J. Dolleman, S. Trelenkamp, F. Lentz, K. Watanabe, T. Taniguchi, D. M. Kennes, B. Beschoten, C. Stampfer, and F. Libisch, Band gap formation in commensurate twisted bilayer graphene/hbn moiré lattices, *Phys. Rev. B* **109**, 155139 (2024).
- [32] C. Mora, N. Regnault, and B. A. Bernevig, Flatbands and perfect metal in trilayer moiré graphene, *Physical review letters* **123**, 026402 (2019).
- [33] Z. Zhu, S. Carr, D. Massatt, M. Luskin, and E. Kaxiras, Twisted trilayer graphene: A precisely tunable platform for correlated electrons, *Physical review letters* **125**, 116404 (2020).
- [34] Z. Zhu, P. Cazeaux, M. Luskin, and E. Kaxiras, Modeling mechanical relaxation in incommensurate trilayer van der waals heterostructures, *Physical Review B* **101**, 224107 (2020).
- [35] X. Zhang, K.-T. Tsai, Z. Zhu, W. Ren, Y. Luo, S. Carr, M. Luskin, E. Kaxiras, and K. Wang, Correlated insulating states and transport signature of superconductivity in twisted trilayer graphene superlattices, *Physical review letters* **127**, 166802 (2021).
- [36] T. Devakul, P. J. Ledwith, L.-Q. Xia, A. Uri, S. C. de la Barrera, P. Jarillo-Herrero, and L. Fu, Magic-angle helical trilayer graphene, *Science Advances* **9**, eadi6063 (2023).
- [37] N. Nakatsuji, T. Kawakami, and M. Koshino, Multi-scale lattice relaxation in general twisted trilayer graphenes (2023), arXiv:2305.13155 [cond-mat.mes-hall].
- [38] D. Guerci, Y. Mao, and C. Mora, Chern mosaic and ideal flat bands in equal-twist trilayer graphene (2023), arXiv:2305.03702 [cond-mat.mes-hall].
- [39] Y. Mao, D. Guerci, and C. Mora, Supermoiré low-energy effective theory of twisted trilayer graphene, *Physical Review B* **107**, 125423 (2023).
- [40] F. K. Popov and G. Tarnopolsky, Magic angles in equal-twist trilayer graphene, arXiv preprint arXiv:2303.15505 (2023).
- [41] F. K. Popov and G. Tarnopolsky, Magic angle butterfly in twisted trilayer graphene, *Physical Review Research* **5**, 043079 (2023).
- [42] D. Foo, Z. Zhan, M. M. Al Ezzi, L. Peng, S. Adam, and F. Guinea, Extended magic phase in twisted graphene multilayers, *Physical Review Research* **6**, 013165 (2024).
- [43] D. Guerci, Y. Mao, and C. Mora, Nature of even and odd magic angles in helical twisted trilayer graphene (2023), arXiv:2308.02638 [cond-mat.mes-hall].
- [44] M. Long, A. Jimeno-Pozo, H. Sainz-Cruz, P. A. Pantaleon, and F. Guinea, Evolution of superconductivity in twisted graphene multilayers, arXiv preprint arXiv:2403.00903 (2024).
- [45] D. Park, C. Park, E. Ko, K. Yananose, R. Engelke, X. Zhang, K. Davydov, M. Green, S. H. Park, J. H. Lee, *et al.*, Tunable incommensurability and spontaneous symmetry breaking in the reconstructed moiré lattices, arXiv preprint arXiv:2402.15760 (2024).
- [46] W. Ren, K. Davydov, Z. Zhu, J. Ma, K. Watanabe, T. Taniguchi, E. Kaxiras, M. Luskin, and K. Wang, Tunable inter-moiré physics in consecutively-twisted trilayer graphene, arXiv preprint arXiv:2311.10313 (2023).
- [47] I. M. Craig, M. Van Winkle, C. Groschner, K. Zhang, N. Dowlatshahi, Z. Zhu, T. Taniguchi, K. Watanabe, S. M. Griffin, and D. K. Bediako, Local atomic stacking and symmetry in twisted graphene trilayers, *Nature Materials* , 1 (2024).
- [48] C.-Y. Hao, Z. Zhan, P. A. Pantaleón, J.-Q. He, Y.-X. Zhao, K. Watanabe, T. Taniguchi, F. Guinea, and L. He, Robust flat bands in twisted trilayer graphene quasicrystals, arXiv preprint arXiv:2401.09010 (2024).
- [49] A. Uri, S. C. de la Barrera, M. T. Randeria, D. Rodan-Legrain, T. Devakul, P. J. Crowley, N. Paul, K. Watanabe, T. Taniguchi, R. Lifshitz, *et al.*, Superconductivity and strong interactions in a tunable moiré quasiperiodic crystal, arXiv preprint arXiv:2302.00686 (2023).
- [50] C. Yang, J. May-Mann, Z. Zhu, and T. Devakul, Multi-moiré trilayer graphene: lattice relaxation, electronic structure, and magic angles, arXiv preprint arXiv:2310.12961 (2023).
- [51] L.-Q. Xia, S. C. de la Barrera, A. Uri, A. Sharpe, Y. H. Kwan, Z. Zhu, K. Watanabe, T. Taniguchi, D. Goldhaber-Gordon, L. Fu, T. Devakul, and P. Jarillo-Herrero, Helical trilayer graphene: a moiré platform for strongly-interacting topological bands (2023), arXiv:2310.12204 [cond-mat.mes-hall].
- [52] Y. H. Kwan, P. J. Ledwith, C. F. B. Lo, and T. Devakul, Strong-coupling topological states and phase transitions in helical trilayer graphene, *Phys. Rev. B* **109**, 125141 (2024).
- [53] A. Dunbrack and J. Cano, Intrinsically multilayer moiré heterostructures, *Physical Review B* **107**, 235425 (2023).
- [54] S. Grover, M. Bocarsly, A. Uri, P. Stepanov, G. Di Battista, I. Roy, J. Xiao, A. Y. Meltzer, Y. Myasoedov, K. Pareek, K. Watanabe, T. Taniguchi, B. Yan, A. Stern, E. Berg, D. K. Efetov, and E. Zeldov, Chern mosaic and berry-curvature magnetism in magic-angle graphene, *Nature Physics* **18**, 885–892 (2022).
- [55] J. Shi, J. Zhu, and A. H. MacDonald, Moiré commensurability and the quantum anomalous hall effect in twisted bilayer graphene on hexagonal boron nitride, *Phys. Rev. B* **103**, 075122 (2021).
- [56] D. Guerci, Y. Mao, and C. Mora, Chern mosaic and ideal flat bands in equal-twist trilayer graphene, *Phys. Rev. Res.* **6**, L022025 (2024).
- [57] J. Shin, Y. Park, B. L. Chittari, J.-H. Sun, and J. Jung, Electron-hole asymmetry and band gaps of commensurate double moire patterns in twisted bilayer graphene on hexagonal boron nitride, *Phys. Rev. B* **103**, 075423 (2021).
- [58] Y. H. Kwan, G. Wagner, N. Chakraborty, S. H. Simon, and S. Parameswaran, Domain wall competition in the chern insulating regime of twisted bilayer graphene, *Physical Review B* **104**, 115404 (2021).
- [59] G. Shavit and Y. Oreg, Domain formation driven by the entropy of topological edge modes, *Phys. Rev. Lett.* **128**, 156801 (2022).
- [60] S. A. Parameswaran, R. Roy, and S. L. Sondhi, Fractional quantum Hall physics in topological flat bands, *Comptes Rendus Physique* **14**, 816 (2013).

- [61] E. J. Bergholtz and Z. Liu, Topological flat band models and fractional chern insulators, *International Journal of Modern Physics B* **27**, 1330017 (2013).
- [62] Z. Liu and E. J. Bergholtz, Recent Developments in Fractional Chern Insulators (2022), arxiv:2208.08449 [cond-mat, physics:math-ph, physics:quant-ph].
- [63] T. Neupert, L. Santos, C. Chamon, and C. Mudry, Fractional Quantum Hall States at Zero Magnetic Field, *Physical Review Letters* **106**, 236804 (2011).
- [64] D. Sheng, Z.-C. Gu, K. Sun, and L. Sheng, Fractional quantum Hall effect in the absence of Landau levels, *Nature Communications* **2**, 389 (2011).
- [65] N. Regnault and B. A. Bernevig, Fractional Chern Insulator, *Physical Review X* **1**, 021014 (2011).
- [66] K. Sun, Z. Gu, H. Katsura, and S. Das Sarma, Nearly flatbands with nontrivial topology, *Phys. Rev. Lett.* **106**, 236803 (2011).
- [67] J. C. Hoke, Y. Li, Y. Hu, J. May-Mann, K. Watanabe, T. Taniguchi, T. Devakul, and B. E. Feldman, Imaging supermoire relaxation and conductive domain walls in helical trilayer graphene (2024), arXiv:2410.16269 [cond-mat.mes-hall].
- [68] M. Koshino, Interlayer interaction in general incommensurate atomic layers, *New Journal of Physics* **17**, 015014 (2015).
- [69] R. Bistritzer and A. H. MacDonald, Moiré bands in twisted double-layer graphene, *Proceedings of the National Academy of Sciences* **108**, 12233 (2011).
- [70] N. Bultinck, E. Khalaf, S. Liu, S. Chatterjee, A. Vishwanath, and M. P. Zaletel, Ground state and hidden symmetry of magic-angle graphene at even integer filling, *Physical Review X* **10**, 031034 (2020).
- [71] B. Lian, Z.-D. Song, N. Regnault, D. K. Efetov, A. Yazdani, and B. A. Bernevig, TBG IV: Exact insulator ground states and phase diagram of twisted bilayer graphene, arXiv preprint arXiv:2009.13530 (2020), arxiv:2009.13530.
- [72] P. J. Ledwith, E. Khalaf, and A. Vishwanath, Strong coupling theory of magic-angle graphene: A pedagogical introduction, *Annals of Physics* **435**, 168646 (2021).
- [73] Z. Wang, Y. H. Kwan, G. Wagner, S. H. Simon, N. Bultinck, and S. A. Parameswaran, Chern-textured exciton insulators with valley spiral order in moiré materials (2024), arXiv:2406.15342 [cond-mat.str-el].
- [74] Y. Xie, A. T. Pierce, J. M. Park, D. E. Parker, E. Khalaf, P. Ledwith, Y. Cao, S. H. Lee, S. Chen, P. R. Forrester, K. Watanabe, T. Taniguchi, A. Vishwanath, P. Jarillo-Herrero, and A. Yacoby, Fractional Chern insulators in magic-angle twisted bilayer graphene, *Nature* **600**, 439 (2021).
- [75] J. Yu, B. A. Foutty, Z. Han, M. E. Barber, Y. Schattner, K. Watanabe, T. Taniguchi, P. Phillips, Z.-X. Shen, S. A. Kivelson, *et al.*, Correlated hofstadter spectrum and flavour phase diagram in magic-angle twisted bilayer graphene, *Nature Physics* **18**, 825 (2022).
- [76] J. Yu, B. A. Foutty, Y. H. Kwan, M. E. Barber, K. Watanabe, T. Taniguchi, Z.-X. Shen, S. A. Parameswaran, and B. E. Feldman, Spin skyrmion gaps as signatures of intervalley-coherent insulators in magic-angle twisted bilayer graphene (2022), arXiv:2206.11304 [cond-mat.mes-hall].
- [77] D. Wong, K. P. Nuckolls, M. Oh, B. Lian, Y. Xie, S. Jeon, K. Watanabe, T. Taniguchi, B. A. Bernevig, and A. Yazdani, Cascade of electronic transitions in magic-angle twisted bilayer graphene, *Nature* **582**, 198 (2020).
- [78] Y. Choi, H. Kim, Y. Peng, A. Thomson, C. Lewandowski, R. Polski, Y. Zhang, H. S. Arora, K. Watanabe, T. Taniguchi, *et al.*, Correlation-driven topological phases in magic-angle twisted bilayer graphene, *Nature* **589**, 536 (2021).
- [79] Y. Choi, H. Kim, C. Lewandowski, Y. Peng, A. Thomson, R. Polski, Y. Zhang, K. Watanabe, T. Taniguchi, J. Alicea, and S. Nadj-Perge, Interaction-driven band flattening and correlated phases in twisted bilayer graphene (2021), arXiv:2102.02209 [cond-mat.str-el].
- [80] K. P. Nuckolls, R. L. Lee, M. Oh, D. Wong, T. Soejima, J. P. Hong, D. Călugăru, J. Herzog-Arbeitman, B. A. Bernevig, K. Watanabe, *et al.*, Quantum textures of the many-body wavefunctions in magic-angle graphene, *Nature* **620**, 525 (2023).
- [81] H. Kim, Y. Choi, Étienne Lantagne-Hurtubise, C. Lewandowski, A. Thomson, L. Kong, H. Zhou, E. Baum, Y. Zhang, L. Holleis, K. Watanabe, T. Taniguchi, A. F. Young, J. Alicea, and S. Nadj-Perge, Imaging inter-valley coherent order in magic-angle twisted trilayer graphene (2023), arXiv:2304.10586 [cond-mat.str-el].
- [82] S. Turkel, J. Swann, Z. Zhu, M. Christos, K. Watanabe, T. Taniguchi, S. Sachdev, M. S. Scheurer, E. Kaxiras, C. R. Dean, *et al.*, Orderly disorder in magic-angle twisted trilayer graphene, *Science* **376**, 193 (2022).
- [83] K. P. Nuckolls, M. Oh, D. Wong, B. Lian, K. Watanabe, T. Taniguchi, B. A. Bernevig, and A. Yazdani, Strongly correlated Chern insulators in magic-angle twisted bilayer graphene, *Nature* **588**, 610 (2020).
- [84] C. Zhang, T. Zhu, T. Soejima, S. Kahn, K. Watanabe, T. Taniguchi, A. Zettl, F. Wang, M. P. Zaletel, and M. F. Crommie, Local spectroscopy of a gate-switchable moiré quantum anomalous hall insulator, *Nature Communications* **14**, 3595 (2023).
- [85] J. C. Slater and G. F. Koster, Simplified lcao method for the periodic potential problem, *Physical review* **94**, 1498 (1954).
- [86] P. Moon and M. Koshino, Optical absorption in twisted bilayer graphene, *Physical Review B—Condensed Matter and Materials Physics* **87**, 205404 (2013).
- [87] P. Wilhelm, T. C. Lang, and A. M. Läuchli, Interplay of fractional chern insulator and charge density wave phases in twisted bilayer graphene, *Phys. Rev. B* **103**, 125406 (2021).
- [88] J. Yu, J. Herzog-Arbeitman, M. Wang, O. Vafek, B. A. Bernevig, and N. Regnault, Fractional chern insulators versus nonmagnetic states in twisted bilayer mote₂, *Phys. Rev. B* **109**, 045147 (2024).
- [89] C. Xu, J. Li, Y. Xu, Z. Bi, and Y. Zhang, Maximally localized wannier functions, interaction models, and fractional quantum anomalous hall effect in twisted bilayer mote₂, *Proceedings of the National Academy of Sciences* **121**, e2316749121 (2024), <https://www.pnas.org/doi/pdf/10.1073/pnas.2316749121>.
- [90] A. Abouelkomsan, A. P. Reddy, L. Fu, and E. J. Bergholtz, Band mixing in the quantum anomalous hall regime of twisted semiconductor bilayers, *Phys. Rev. B* **109**, L121107 (2024).
- [91] J. Yu, J. Herzog-Arbeitman, Y. H. Kwan, N. Regnault, and B. A. Bernevig, Moiré fractional chern insulators iv: Fluctuation-driven collapse of fcis in multi-band exact diagonalization calculations on rhombohedral graphene

- (2024), arXiv:2407.13770 [cond-mat.str-el].
- [92] Y. H. Kwan, G. Wagner, J. Yu, A. K. Dagnino, Y. Jiang, X. Xu, B. A. Bernevig, T. Neupert, and N. Regnault, When could abelian fractional topological insulators exist in twisted $m\tau_2$ (and other systems) (2024), arXiv:2407.02560 [cond-mat.str-el].
- [93] E. H. Rezayi and S. H. Simon, Breaking of particle-hole symmetry by Landau level mixing in the $\nu = 5/2$ quantized Hall state, Phys. Rev. Lett. **106**, 116801 (2011).

Appendix A: Derivation of momentum dependent tunneling term

In this Appendix, we give a derivation of the momentum dependent tunneling (MDT) term used in the main text. For simplicity, consider twisted bilayer graphene with a small twist angle θ . The generalization to trilayer is straightforward.

Each graphene layer is described by a honeycomb lattice tight binding model with the two sublattices labeled $\sigma \in \{A, B\}$. We keep spin labels implicit. Working in momentum space, states in the layer $\ell = 1, 2$ are labeled by

$$|\mathbf{k}, \sigma, \ell\rangle = \frac{1}{\sqrt{N}} \sum_{\mathbf{R}_{\sigma\ell}} e^{i\mathbf{k}\cdot\mathbf{R}_{\sigma\ell}} |\mathbf{R}_{\sigma\ell}, \sigma, \ell\rangle \quad (\text{A1})$$

where $\mathbf{R}_{\sigma\ell}$ are the locations of the sublattice σ sites on layer ℓ , $|\mathbf{R}_{\sigma\ell}, \sigma, \ell\rangle$ is the corresponding state, and N is the total number of unit cells. We assume the system is large but finite in order to properly normalize the wavefunctions. Here, \mathbf{k} is a crystal momentum defined within the monolayer Brillouin zone of layer ℓ , so $|\mathbf{k} + \mathbf{G}_\ell, \sigma, \ell\rangle \equiv |\mathbf{k}, \sigma, \ell\rangle$ where \mathbf{G}_ℓ is a monolayer reciprocal lattice vector of layer ℓ . The inverse Fourier transform is

$$|\mathbf{R}_{\sigma\ell}, \sigma, \ell\rangle = \frac{1}{\sqrt{N}} \sum_{\mathbf{k}} e^{-i\mathbf{k}\cdot\mathbf{R}_{\sigma\ell}} |\mathbf{k}, \sigma, \ell\rangle. \quad (\text{A2})$$

where the sum is over momenta \mathbf{k} within the appropriate Brillouin zone. The intralayer Hamiltonian acts within each layer and gives rise to the usual monolayer graphene dispersions.

We are concerned with the interlayer tunneling. Consider a general tunneling matrix element that depends only on the distance between the initial and final states (the two-center approximation),

$$H_{\text{inter}} = \sum_{\sigma'\sigma} \sum_{\mathbf{R}_{\sigma 1} \mathbf{R}_{\sigma 2}} W(\mathbf{R}_{\sigma' 2} - \mathbf{R}_{\sigma 1}) |\mathbf{R}_{\sigma' 2}, \sigma', 2\rangle \langle \mathbf{R}_{\sigma 1}, \sigma, 1| + h.c. \quad (\text{A3})$$

where $W(\mathbf{r})$ is the hopping amplitude which decays with in-plane distance r . Inserting the inverse Fourier transform, we have

$$H_{\text{inter}} = \frac{1}{N} \sum_{\sigma'\sigma} \sum_{\mathbf{R}_{\sigma 1} \mathbf{R}_{\sigma 2}} \sum_{\mathbf{k}' \in \text{BZ}_2} \sum_{\mathbf{k} \in \text{BZ}_1} e^{-i\mathbf{k}'\cdot\mathbf{R}_{\sigma' 2} + i\mathbf{k}\cdot\mathbf{R}_{\sigma 1}} W(\mathbf{R}_{\sigma' 2} - \mathbf{R}_{\sigma 1}) |\mathbf{k}', \sigma', 2\rangle \langle \mathbf{k}, \sigma, 1| + h.c. \quad (\text{A4})$$

On a finite periodic system, the tunneling amplitude $W(\mathbf{r})$ should also be a periodic function of \mathbf{r} . This means we should replace $W(\mathbf{r}) \rightarrow W_{\text{per}}(\mathbf{r})$ with some periodic function $W_{\text{per}}(\mathbf{r} + \mathbf{L}) = W_{\text{per}}(\mathbf{r})$ where \mathbf{L} is any vector connecting a site with its periodic image. A periodic tunneling can be constructed as $W_{\text{per}}(\mathbf{r}) = \sum_{\mathbf{L}} W(\mathbf{r} + \mathbf{L})$ where the sum is over the lattice of all \mathbf{L} . Define the continuum Fourier transform for the original hopping amplitude

$$\begin{aligned} \tilde{W}(\mathbf{q}) &= \frac{1}{A_{\text{uc}}} \int d\mathbf{r} e^{-i\mathbf{q}\cdot\mathbf{r}} W(\mathbf{r}) \\ W(\mathbf{r}) &= A_{\text{uc}} \int \frac{d\mathbf{q}}{4\pi^2} e^{i\mathbf{q}\cdot\mathbf{r}} \tilde{W}(\mathbf{q}) \end{aligned} \quad (\text{A5})$$

where A_{uc} is the monolayer graphene unit cell area. This leads to

$$W_{\text{per}}(\mathbf{r}) = \sum_{\mathbf{L}} W(\mathbf{r} + \mathbf{L}) = A_{\text{uc}} \sum_{\mathbf{L}} \int \frac{d\mathbf{q}}{4\pi^2} e^{i\mathbf{q}\cdot\mathbf{L}} e^{i\mathbf{q}\cdot\mathbf{r}} \tilde{W}(\mathbf{q}) = \frac{1}{N} \sum_{\mathbf{q}} \tilde{W}(\mathbf{q}) e^{i\mathbf{q}\cdot\mathbf{r}} \quad (\text{A6})$$

where the sum over \mathbf{q} in the final line is over the discrete momenta commensurate with the system size \mathbf{L} , and we have used $\sum_{\mathbf{L}} e^{i\mathbf{k}\cdot\mathbf{L}} = \frac{1}{NA_{\text{uc}}} \sum_{\mathbf{q}} 4\pi^2 \delta^{(2)}(\mathbf{k} - \mathbf{q})$, with $\delta^{(2)}$ the two-dimensional Dirac delta function.

The interlayer hopping can then be expressed

$$H_{\text{inter}} = \frac{1}{N^2} \sum_{\mathbf{q}} \sum_{\sigma'\sigma} \sum_{\mathbf{R}_{\sigma 1} \mathbf{R}_{\sigma 2}} \sum_{\mathbf{k}' \in \text{BZ}_2} \sum_{\mathbf{k} \in \text{BZ}_1} e^{-i(\mathbf{k}' - \mathbf{q})\cdot\mathbf{R}_{\sigma' 2} + i(\mathbf{k} - \mathbf{q})\cdot\mathbf{R}_{\sigma 1}} \tilde{W}(\mathbf{q}) |\mathbf{k}', \sigma', 2\rangle \langle \mathbf{k}, \sigma, 1| + h.c. \quad (\text{A7})$$

Next, we can use that $\sum_{\mathbf{R}_{\sigma\ell}} e^{i\mathbf{k}\cdot\mathbf{R}_{\sigma\ell}} = N e^{i\mathbf{k}\cdot\boldsymbol{\tau}_{\sigma\ell}} \sum_{\mathbf{G}_\ell} \delta_{\mathbf{k}, \mathbf{G}_\ell}$ where $\boldsymbol{\tau}_{\sigma\ell}$ is the offset of the lattice of $\mathbf{R}_{\sigma\ell}$ from the origin (for graphene, this encodes the offset between the A and B sublattices). This results in a sum over \mathbf{G}_1 and \mathbf{G}_2 and Kronecker deltas $\delta_{\mathbf{k}' - \mathbf{q}, \mathbf{G}_2}$ and $\delta_{\mathbf{k} - \mathbf{q}, \mathbf{G}_1}$,

$$H_{\text{inter}} = \sum_{\sigma'\sigma} \sum_{\mathbf{q}} \sum_{\mathbf{G}_2, \mathbf{G}_1} \sum_{\mathbf{k}' \in \text{BZ}_2} \sum_{\mathbf{k} \in \text{BZ}_1} e^{-i\mathbf{G}_2\cdot\boldsymbol{\tau}_{\sigma' 2} + i\mathbf{G}_1\cdot\boldsymbol{\tau}_{\sigma 1}} \delta_{\mathbf{k}' - \mathbf{q}, \mathbf{G}_2} \delta_{\mathbf{k} - \mathbf{q}, \mathbf{G}_1} \tilde{W}(\mathbf{q}) |\mathbf{k}', \sigma', 2\rangle \langle \mathbf{k}, \sigma, 1| + h.c. \quad (\text{A8})$$

Performing the sum over \mathbf{q} and relabeling $\mathbf{G}_\ell \rightarrow -\mathbf{G}_\ell$ in the sum finally leads to

$$H_{\text{inter}} = \sum_{\sigma'\sigma} \sum_{\mathbf{G}_2, \mathbf{G}_1} \sum_{\mathbf{k}' \in \text{BZ}_2} \sum_{\mathbf{k} \in \text{BZ}_1} e^{i\mathbf{G}_2 \cdot \boldsymbol{\tau}_{\sigma'2} - i\mathbf{G}_1 \cdot \boldsymbol{\tau}_{\sigma 1}} \delta_{\mathbf{k} + \mathbf{G}_1, \mathbf{k}' + \mathbf{G}_2} \tilde{W}(\mathbf{k} + \mathbf{G}_1) |\mathbf{k}', \sigma', 2\rangle \langle \mathbf{k}, \sigma, 1| + h.c. \quad (\text{A9})$$

Note that for physically realistic tunneling, $\tilde{W}(\mathbf{q}) \rightarrow 0$ as $|\mathbf{q}| \rightarrow \infty$ so the physics will be dominated tunneling events that occur with the smallest $|\mathbf{k} + \mathbf{G}_1| = |\mathbf{k}' + \mathbf{G}_2|$.

Our discussion until now has been quite general for two-layer systems. Let us now specialize to graphene and focus on the low energy physics near the K points and small twist angle θ .

Let us define $\mathbf{K} = \frac{4\pi}{3a_0}(1, 0)$ to be the K -point for an untwisted monolayer graphene, and $\mathbf{b}_1 = \frac{4\pi}{\sqrt{3}a_0}(-\frac{\sqrt{3}}{2}, \frac{1}{2})$ and $\mathbf{b}_2 = \frac{4\pi}{\sqrt{3}a_0}(-\frac{\sqrt{3}}{2}, -\frac{1}{2})$ to be two generators of the reciprocal lattice, i.e. $\mathbf{G} = n_1\mathbf{b}_1 + n_2\mathbf{b}_2$ with integers n_1, n_2 . They are defined such that the C_{3z} symmetry related \mathbf{K} points are

$$\mathbf{R}(\frac{2\pi}{3})\mathbf{K} = \mathbf{K} + \mathbf{b}_1; \quad \mathbf{R}(\frac{4\pi}{3})\mathbf{K} = \mathbf{K} + \mathbf{b}_2 \quad (\text{A10})$$

where $\mathbf{R}(\phi)$ is the counter-clockwise rotation matrix by angle ϕ . We define the layer ℓ K -point to be $\mathbf{K}_\ell = \mathbf{R}(\theta_\ell)\mathbf{K}$, and reciprocal lattice vectors $(\mathbf{b}_{\ell 1}, \mathbf{b}_{\ell 2}) = \mathbf{R}(\theta_\ell)(\mathbf{b}_1, \mathbf{b}_2)$, with $\theta_1 = -\theta_2 = \theta/2$.

The low energy physics in graphene occurs near the \mathbf{K} points. Let us parameterize momenta near the \mathbf{K}_ℓ point by $\mathbf{p}_\ell = \mathbf{k} - \mathbf{K}_\ell$, where $|\mathbf{p}_\ell|$ is always much smaller than any (non-zero) reciprocal lattice vector. Consider the state $|\mathbf{k}, \sigma, 1\rangle$ near the \mathbf{K}_1 point. To find all the terms that couple to it, note that for any given \mathbf{G}_1 , both \mathbf{k}' and \mathbf{G}_2 are uniquely fixed by the Kronecker delta $\mathbf{k} + \mathbf{G}_1 = \mathbf{k}' + \mathbf{G}_2$ since $\mathbf{k}' \in \text{BZ}_2$ lives only in the first BZ. So, we only need to consider the possible choices of \mathbf{G}_1 , for which we can assign a unique tunneling amplitude $\tilde{W}(\mathbf{k} + \mathbf{G}_1)$. There are three choices for which $|\mathbf{k} + \mathbf{G}_1|$ is smallest, known as the ‘‘first harmonics’’:

$$\begin{aligned} (0) : \mathbf{G}_1 = 0 &\implies |\mathbf{k} + \mathbf{G}_1| = |\mathbf{p}_1 + \mathbf{K}_1| \\ (1) : \mathbf{G}_1 = \mathbf{b}_{1,1} &\implies |\mathbf{k} + \mathbf{G}_1| = |\mathbf{p}_1 + \mathbf{R}(\frac{2\pi}{3})\mathbf{K}_1| \\ (2) : \mathbf{G}_1 = \mathbf{b}_{1,2} &\implies |\mathbf{k} + \mathbf{G}_1| = |\mathbf{p}_1 + \mathbf{R}(\frac{4\pi}{3})\mathbf{K}_1|. \end{aligned} \quad (\text{A11})$$

The hopping matrix elements in Eq. A9 send $|\mathbf{p}_1 + \mathbf{K}_1, \sigma, 1\rangle \rightarrow |\mathbf{p}_1 + \mathbf{K}_1 + \mathbf{G}_1 - \mathbf{G}_2, \sigma', 2\rangle \equiv |\mathbf{p}_2 + \mathbf{K}_2, \sigma', 2\rangle$ where \mathbf{G}_2 should be chosen so that \mathbf{p}_2 remains a small momentum. This amounts to letting $\mathbf{G}_2 = 0, \mathbf{b}_{2,1}$, and $\mathbf{b}_{2,2}$ for the three tunneling terms listed above. These three tunneling matrix elements, labeled $n = 0, 1, 2$, therefore send $\mathbf{p}_1 \rightarrow \mathbf{p}_2 = \mathbf{p}_1 + \mathbf{K}_1 - \mathbf{K}_2 + \mathbf{G}_1 - \mathbf{G}_2 \equiv \mathbf{p}_1 + \mathbf{q}_n$ where

$$\mathbf{q}_0 = \mathbf{K}_1 - \mathbf{K}_2; \quad \mathbf{q}_1 = \mathbf{K}_1 - \mathbf{K}_2 + \mathbf{b}_{1,1} - \mathbf{b}_{2,1}; \quad \mathbf{q}_2 = \mathbf{K}_1 - \mathbf{K}_2 + \mathbf{b}_{1,2} - \mathbf{b}_{2,2} \quad (\text{A12})$$

characterize the three first harmonic tunneling terms. Notice that $\mathbf{q}_n = \mathbf{R}(\frac{2\pi n}{3})\mathbf{q}_0$ are related to each other by rotations. From Eq. A11, these three terms occur with the tunneling amplitudes $\tilde{W}(\mathbf{p}_1 + \mathbf{R}(\frac{2\pi n}{3})\mathbf{K}_1)$.

The Bistritzer-MacDonald continuum model follows from keeping only these three first harmonic terms and approximating the tunneling amplitude by its value at \mathbf{K} : $\tilde{W}(\mathbf{p}_1 + \mathbf{R}(\frac{2\pi n}{3})\mathbf{K}_1) \approx \tilde{W}(\mathbf{K})$. Since the tunneling amplitude does not depend on \mathbf{p}_1 , it is ‘‘momentum independent’’. The momentum dependent tunneling (MDT) term used in the main text incorporates the next leading order correction in this approximation. We now illustrate how this is taken into account.

Let $\bar{\mathbf{K}} = (\mathbf{K}_1 + \mathbf{K}_2)/2$ be an average of the two \mathbf{K} -points (for N_L layers, one would choose the average of all N_L). For each of the three tunneling events, we Taylor expand $\tilde{W}(\mathbf{q})$ near $\mathbf{q} = \mathbf{R}(\frac{2\pi n}{3})\bar{\mathbf{K}}$. The tunneling amplitude then takes the form

$$\tilde{W}(\mathbf{p}_1 + \mathbf{R}(\frac{2\pi n}{3})\mathbf{K}_1) \approx \tilde{W}(\mathbf{R}(\frac{2\pi n}{3})\bar{\mathbf{K}}) + (\mathbf{p}_1 + \mathbf{R}(\frac{2\pi n}{3})(\mathbf{K}_1 - \bar{\mathbf{K}})) \cdot \boldsymbol{\nabla} \tilde{W}(\mathbf{R}(\frac{2\pi n}{3})\bar{\mathbf{K}}) \quad (\text{A13})$$

where $\boldsymbol{\nabla} \tilde{W}$ is the gradient of \tilde{W} .

In twisted bilayer graphene and h-HTG, $\bar{\mathbf{K}}$ points along the x -direction and \mathbf{q}_0 points along the y -direction. If we take $\tilde{W}(\mathbf{k})$ to be rotation symmetric, then it only depends on $|\mathbf{k}|$, and therefore $\boldsymbol{\nabla} \tilde{W}(\bar{\mathbf{K}})$ points in the x direction. Since the three tunneling terms are related by $2\pi/3$ rotations, we see that the tunneling term with \mathbf{q}_n only depends on the magnitude of \mathbf{p}_1 perpendicular to \mathbf{q}_n . Defining $\hat{\mathbf{q}}_{n,\perp} = (\cos \frac{2\pi n}{3}, \sin \frac{2\pi n}{3})$, Eq A13 simplifies to

$$\tilde{W}(\mathbf{p}_1 + \mathbf{R}(\frac{2\pi n}{3})\mathbf{K}_1) \approx w_0(1 + \lambda_{\text{MDT}}\hat{\mathbf{q}}_{n,\perp} \cdot \mathbf{p}_1) \quad (\text{A14})$$

as quoted in the main text. In terms of $\tilde{W}(\mathbf{q})$, we have $w_0 = \tilde{W}(\bar{\mathbf{K}})$ which is the usual (momentum-independent) interlayer tunneling strength in the Bistritzer-MacDonald continuum model, and $\lambda_{\text{MDT}} = (\boldsymbol{\nabla} \tilde{W}(\bar{\mathbf{K}}))_x / w_0$ accounts for the leading order correction.

To estimate the magnitude of λ_{MDT} , we plot in Fig S1 the tunneling amplitude for the Slater-Koster [85] form for $W(\mathbf{r})$ with the parameters used in Ref [68, 86]. We also plot the linear approximation, using $w_0 = w_{AB} = 110\text{meV}$ and $\lambda_{\text{MDT}} = -2.3\text{\AA}$ as used in the main text for the AB interlayer tunneling. Indeed, this approximation captures the behavior of $\tilde{W}(q)$ near the K -point at $q \approx 17\text{nm}^{-1}$.

Due to lattice relaxation effects at the moiré scale, the effective inter-sublattice and intra-sublattice tunneling strengths differ. In this work, we incorporate this by scaling the inter-sublattice tunneling by a factor w_{AA}/w_{AB} , where we take $w_{AA} = 75\text{meV}$.

We note that the precise value of λ_{MDT} does not qualitatively affect the interacting results in this work. For example, in Fig. S6, we compare HF calculations using $\lambda_{\text{MDT}} = -2.0\text{\AA}$ and -2.3\AA .

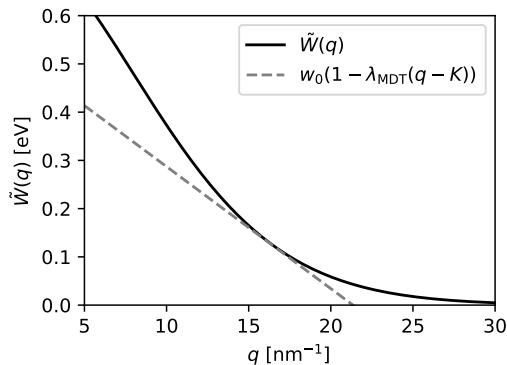


FIG. S1. Plot of $\tilde{W}(q)$, the Fourier transform on the interlayer tunneling amplitude. Dashed line shows the linear approximation which is accurate near the K point of graphene.

Appendix B: Single-particle band structure with and without inter-Chern hybridization

In Fig. S2, we show additional details of the dispersion of the central bands at $\theta = 1.8^\circ$ and vanishing interlayer potential $U = 0\text{meV}$, comparing the cases with and without MDT. In particular, we also consider switching off the inter-Chern hybridization, i.e. we rotate the single-particle dispersion to the Chern-sublattice basis, and neglect the off-diagonal terms in Chern-sublattice space. This procedure provides a concrete definition of the dispersions $E_{\tilde{\sigma}_z}(\mathbf{k})$ of the A and B bands. It can be seen that the B band is significantly more dispersive than the A band regardless of MDT. With MDT though, the B band is generally shifted down compared to the A band, especially near center of the mBZ. The quantum geometric properties of the Chern-sublattice bands are robust to MDT owing to the large remote gaps.

Fig. S3 shows analogous results but with interlayer potential $U = 20\text{meV}$. Note that the interlayer potential U acts as a sublattice diagonal onsite potential with strength $U, 0, -U$ on the top, middle, and bottom layers respectively. Regardless of MDT, the main effect of the displacement field is to raise (lower) the energy of the B band at the mBZ corner κ (κ').

In all plots of single-particle dispersions in this work, we show the band structure relative to the charge neutrality point. For all interacting calculations in this work, we use the full single-particle dispersion that includes the hybridization between the A and B bands.

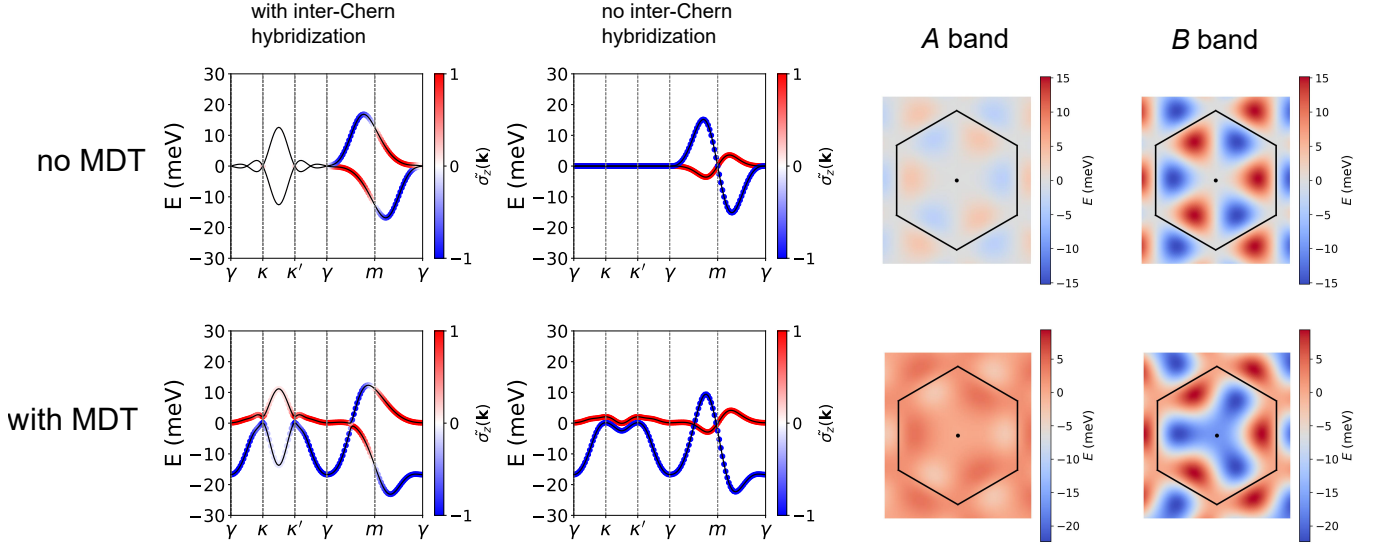


FIG. S2. **Single-particle band structure with and without inter-Chern hybridization at $U = 0$ meV.** Top (bottom) row shows results without (with) MDT. The first and second columns show the dispersion of the central bands with and without inter-Chern hybridization. The color indicates the Chern-sublattice polarization. The third and fourth columns show the A and B band dispersions in the mBZ (black hexagon) without the inter-Chern hybridization. Without MDT, $E_A(\mathbf{k})$ has a mean energy of 0.0 meV and is bounded by -3.6 meV and 3.6 meV, while $E_B(\mathbf{k})$ has a mean energy of 0.0 meV and is bounded by -15.2 meV and 15.2 meV. With MDT, $E_A(\mathbf{k})$ has a mean energy of 1.0 meV and is bounded by -2.9 meV and 4.2 meV, while $E_B(\mathbf{k})$ has a mean energy of -6.4 meV and is bounded by -22.4 meV and 9.4 meV. Twist angle is $\theta = 1.8^\circ$, and interlayer potential is $U = 0$ meV.

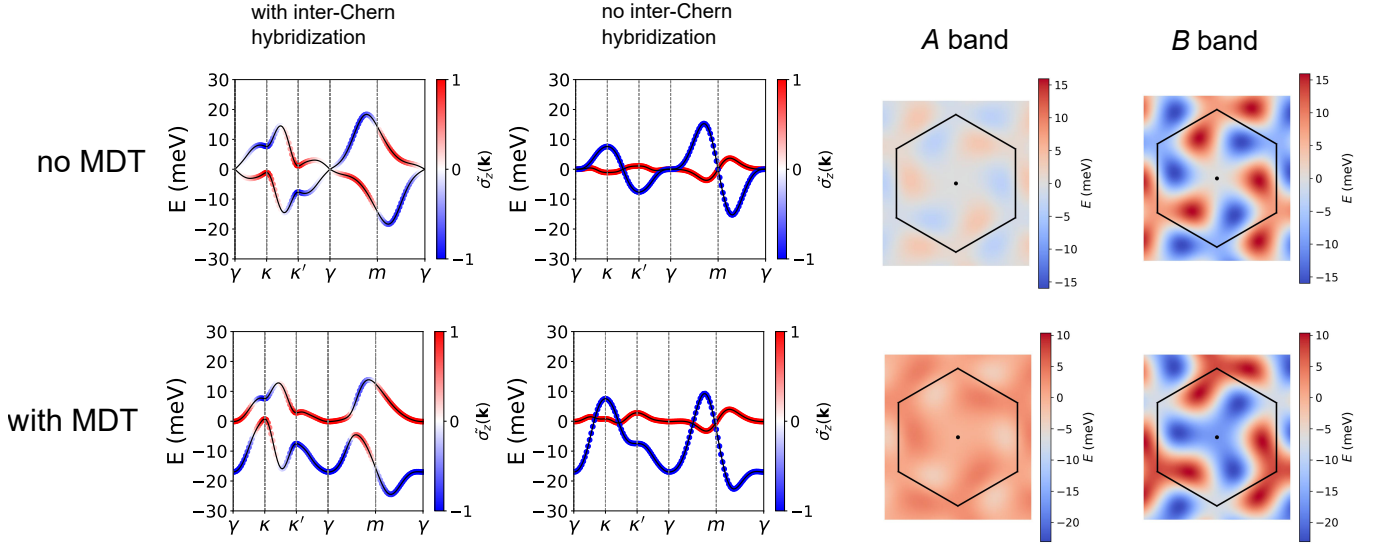


FIG. S3. **Single-particle band structure with and without inter-Chern hybridization at $U = 20$ meV.** Top (bottom) row shows results without (with) MDT. The first and second columns show the dispersion of the central bands with and without inter-Chern hybridization. The color indicates the Chern-sublattice polarization. The third and fourth columns show the A and B band dispersions in the mBZ (black hexagon) without the inter-Chern hybridization. Without MDT, $E_A(\mathbf{k})$ has a mean energy of 0.0 meV and is bounded by -3.7 meV and 3.7 meV, while $E_B(\mathbf{k})$ has a mean energy of 0.0 meV and is bounded by -16.0 meV and 16.0 meV. With MDT, $E_A(\mathbf{k})$ has a mean energy of 0.7 meV and is bounded by -3.3 meV and 4.0 meV, while $E_B(\mathbf{k})$ has a mean energy of -6.6 meV and is bounded by -23.1 meV and 10.4 meV. Twist angle is $\theta = 1.8^\circ$, and interlayer potential is $U = 20$ meV.

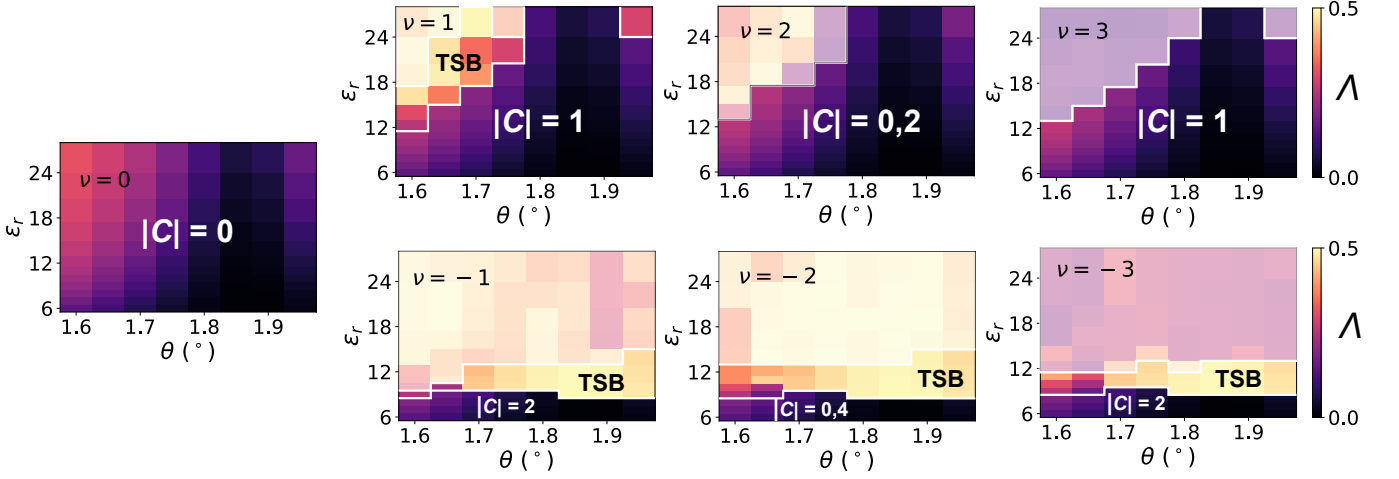


FIG. S4. **Hartree-Fock phase diagram with MDT at all integer fillings.** HF phase diagram as a function of twist angle θ and relative permittivity ϵ_r . White shaded regions indicate gapless states. $\Lambda \equiv \max_{\tau,s,\sigma} \left[\min(\langle n_{\tau,s,\sigma} \rangle, 1 - \langle n_{\tau,s,\sigma} \rangle) \right]$ is a measure of how far the HF solution is from an idealized strong-coupling state. TSB indicates various states that break moiré translation symmetry. System size is 12×12 , and we allow for spontaneous doubling or tripling of the moiré unit cell along both directions. Interlayer potential is $U = 0$.

Appendix C: Additional Hartree-Fock calculations

1. Phase diagrams for other integer fillings

In Fig. S4, we show HF phase diagrams for all non-integer fillings in the presence of MDT. The particle-hole asymmetry is apparent for all non-integer fillings. For positive integer fillings, the strong-coupling insulator occupies the majority of the phase diagram, while for negative integer fillings, it only survives for strong interactions. The Chern numbers can be understood from the principle that starting from band insulator at $\nu = -4$ (with $C = 0$), the system first occupies B bands with $|C| = 2$, then A bands with $|C| = 1$. For $|\nu| = 2$, our HF calculations find that strong-coupling states that differ by the valley polarization are exactly degenerate, which arises from a ‘flavor permutation symmetry’ that holds at mean-field level [52]. For $\nu = 0$, no symmetries are broken, and the system can sustain an indirect HF gap for rather weak interactions.

2. Quantum geometry of the $|C| = 1$ band at $\nu = +3$

In Fig. S5, we compute the Berry curvature $f(\mathbf{k})$ and the trace of the Fubini-Study metric $g_{\text{FS}}(\mathbf{k})$ [60] for the unoccupied $|C| = 1$ HF band of the strong-coupling insulator at $\nu = +3$. The curvature is relatively homogeneous throughout the mBZ, and the violation of the trace condition $\frac{A_{\text{mBZ}}}{2\pi} \int d\mathbf{k} \text{tr}(|g_{\text{FS}}(\mathbf{k})| - |f(\mathbf{k})|)$, where A_{mBZ} is the area of the mBZ, is fairly small. The quantum geometry becomes smoother as the interaction strength is increased.

3. Additional HF data for $3 \leq \nu \leq 4$ Chern-sublattice polarization

In Fig. S6, we show the Chern-sublattice polarization $\langle \tilde{\sigma}_z \rangle$ obtained with HF calculations in the filling range $3 \leq \nu \leq 4$ for additional sets of parameters. The data for $\lambda_{\text{MDT}} = -2.0 \text{ \AA}$ is remarkably similar to that for $\lambda_{\text{MDT}} = -2.3 \text{ \AA}$, which is the default value used in this paper. Application of a moderate interlayer potential $U = 20 \text{ meV}$ leads to a reduction of ν_c .

4. Properties at all fillings

In Fig. S7, we present various properties of the HF solution throughout the narrow-band filling regime $-4 < \nu < +4$. The sublattice polarization $\langle \tilde{\sigma}_z \rangle$ monotonically decreases from 0 for $-4 < \nu < 0$, as the system populates the dispersive

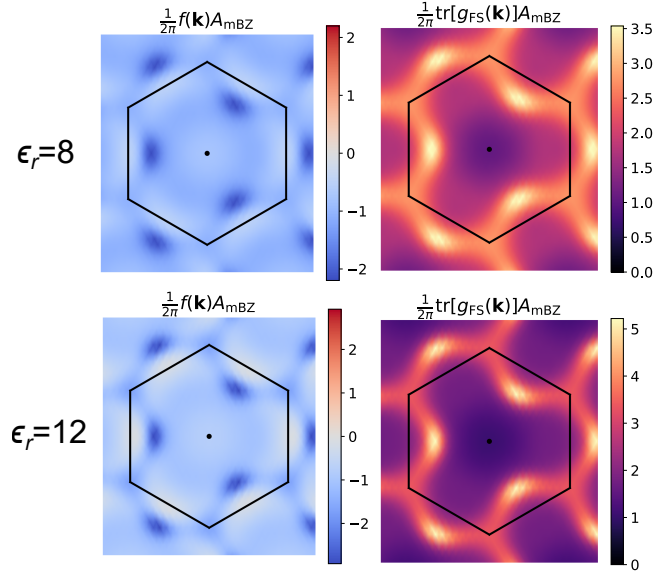


FIG. S5. Quantum geometry of the unoccupied HF $|C| = 1$ band at $\nu = +3$ for $\epsilon_r = 8, 12$. $f(\mathbf{k})$ is the Berry curvature, and $g_{\text{FS}}(\mathbf{k})$ is the Fubini-Study metric. The trace condition violation $\frac{A_{\text{mBZ}}}{2\pi} \int d\mathbf{k} \text{tr}([g_{\text{FS}}(\mathbf{k})] - |f(\mathbf{k})|)$, where A_{mBZ} is the momentum area of the mBZ, is 1.05 and 1.30 for $\epsilon_r = 8, 15$ respectively. System size is 24×24 , $\theta = 1.80^\circ$, and $U = 0$.

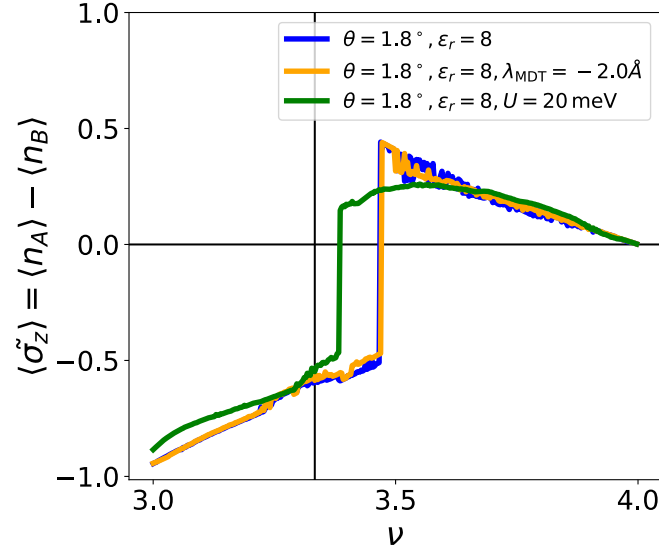


FIG. S6. Additional data for Chern-sublattice polarization in HF. System size is 18×18

B bands with overall lower kinetic energy than the A bands. For $\nu > 0$, we observe a series of sublattice transitions that repeats between every integer filling. $\text{Var}[n_{\tau,s}]$ is the variance of the flavor occupations (i.e. the number of particles with that flavor per moiré unit cell) across the two valleys τ and two spins s , and gives a measure of the degree of flavor polarization. For $\nu < 0$, the $\epsilon_r = 15$ calculation shows only weak flavor polarization. For $\nu > 0$, the data for $\epsilon_r = 8$ and $\epsilon_r = 15$ show qualitatively different behavior, which is due to the fact that the former is in the ‘flavor-imbalanced’ regime with stronger interactions, while the latter is in the ‘flavor-balanced’ regime [52]. However, both interaction strengths yield a fully flavor-polarized state between $\nu = +3$ and the critical filling ν_c at which the sublattice transition in the interval $3 < \nu < 4$ occurs. For $\epsilon_r = 8$, the full flavor polarization persists for a finite window beyond ν_c , implying that the position of the sublattice transition here is not controlled by the flavor physics. μ tracks the chemical potential evolution as a function of ν . There are sharp negative features in the inverse compressibility $\sim \frac{d\mu}{d\nu}$, especially at the sublattice transitions. Note that the overall increase in μ from $\nu = -4$ to

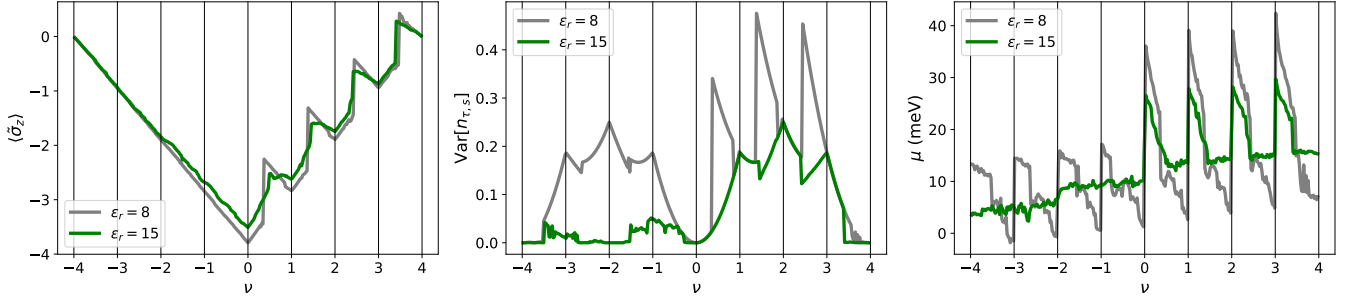


FIG. S7. **Properties of the Hartree-Fock solution with MDT as a function of ν .** We show results for $\epsilon_r = 8, 15$. Left: Chern sublattice polarization $\langle \tilde{\sigma}_z \rangle$. Middle: Variance in the flavor occupations $\text{Var}[n_{\tau,s}]$. Right: Chemical potential. System size is 18×18 , $\theta = 1.80^\circ$, $U = 0$ meV, and translation symmetry and valley $U_v(1)$ is enforced.

$\nu = +4$ is only around ~ 10 meV, which is an indication that Hartree renormalization effects in h-HTG are not large.

5. HF phase diagram at $\nu = +3$ with interlayer potential

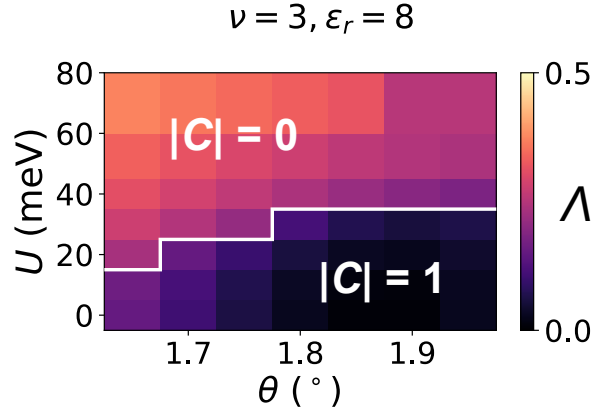


FIG. S8. **Hartree-Fock phase diagram at $\nu = +3$ with MDT and interlayer potential U .** $\Lambda \equiv \max_{\tau,s,\tilde{\sigma}} [\min(\langle n_{\tau,s,\tilde{\sigma}} \rangle, 1 - \langle n_{\tau,s,\tilde{\sigma}} \rangle)]$ is a measure of how far the HF solution is from an idealized strong-coupling state. System size is 12×12 , we fix $\epsilon_r = 8$, and we enforce moiré translation invariance.

In Fig. S8, we show the HF phase diagram with $\nu = +3$ in the presence of MDT and an interlayer potential U for $\epsilon_r = 8$. For $U \lesssim 30$ meV, we find a strong-coupling $|C| = 1$ insulator, which undergoes a displacement-field-tuned transition to a $|C| = 0$ insulator that does not fit the strong-coupling framework [52]. This $|C| = 0$ state can be understood as arising from momentum-local sublattice inversions. Note that at even higher U , we expect to find various intervalley-coherent and translation symmetry-broken phases, but we enforce valley $U(1)_v$ and moiré translation symmetry here for simplicity.

Appendix D: Additional exact diagonalization calculations

1. Calculations for $\theta = 1.8^\circ$ with displacement field

Fig. S9 and S10 show additional $\nu = 3 + \frac{1}{3}$ ED data performed at $\theta = 1.8^\circ$ with finite interlayer potential U and $\epsilon_r = 8$. For a wide range of displacement fields $|U| < 30$ meV, 1-band ED shows good evidence of an FCI. However, Fig. S10 demonstrates that a sufficiently large displacement field can undermine the sublattice-Chern polarization, which makes restriction to a single active HF band less justified.

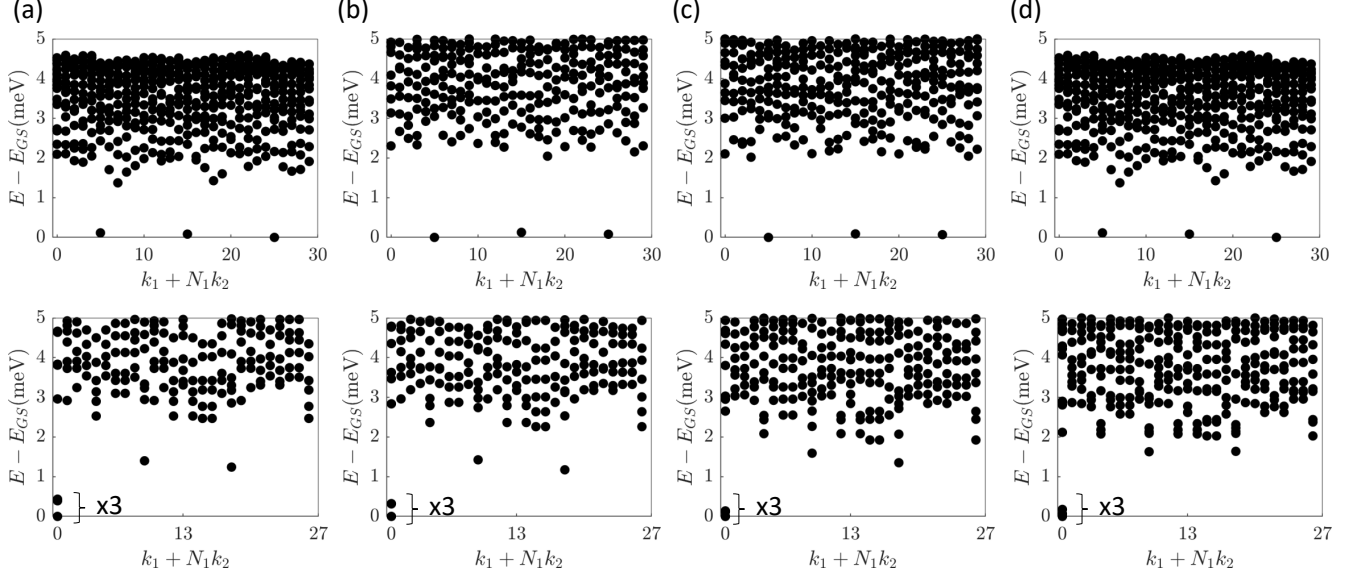


FIG. S9. 1-band ED calculations at $\nu = 3 + \frac{1}{3}$ at finite interlayer potential U . We fix $\theta = 1.8^\circ$ and $\epsilon_r = 8$ for all plots. Top row is for the 5×6 site cluster, and bottom row is for the tilted 27 site cluster. Interlayer potential U is (a) 5 meV, (b) 10 meV, (c) 20 meV, and (d) 30 meV.

2. Calculations for $\theta = 1.8^\circ$ without displacement field

Fig. S11a shows the many-body spectrum of 2-band ED performed on the 3×4 cluster at $\nu = 3$. There is a single non-degenerate ground state, separated by a neutral gap of around 10 meV and 5 meV for $\epsilon_r = 8$ and $\epsilon_r = 15$ respectively. The top row of Fig. S11a shows the eigenvalues of the occupation matrix $n_{ij}(\mathbf{k})$ of this ground state (i, j index the two bands). The two branches of the eigenvalues are close to either 0 or 1, demonstrating that the ground state at $\nu = 3$ is effectively a single Slater determinant state that is polarized in the A band.

Fig. S11b plots the occupation number $n(\mathbf{k})$ of the ground state obtained from 1-band ED at $\nu = 3 + 1/3$. There is still considerable fluctuation in $n(\mathbf{k})$ among different \mathbf{k} . This suggests that the competition from the kinetic energy is still important, and may be an important source of finite-size effects observed in our ED calculations.

3. Calculations for $\theta = 1.85^\circ$

Fig. S12 shows additional ED data at twist angle $\theta = 1.85^\circ$. 1-band ED performed on the 5×6 cluster shows clear signs of an FCI, as indicated by the 3-fold quasi-degenerate ground states that evolve into each other and remain gapped from higher states under flux threading. However, calculations performed on the tilted 27-site lattice [87] show that there are competing excitations at κ and κ' . This should be compared with the result at $\theta = 1.8^\circ$, where there are three quasi-degenerate ground states at γ and the possibility of charge density wave is excluded.

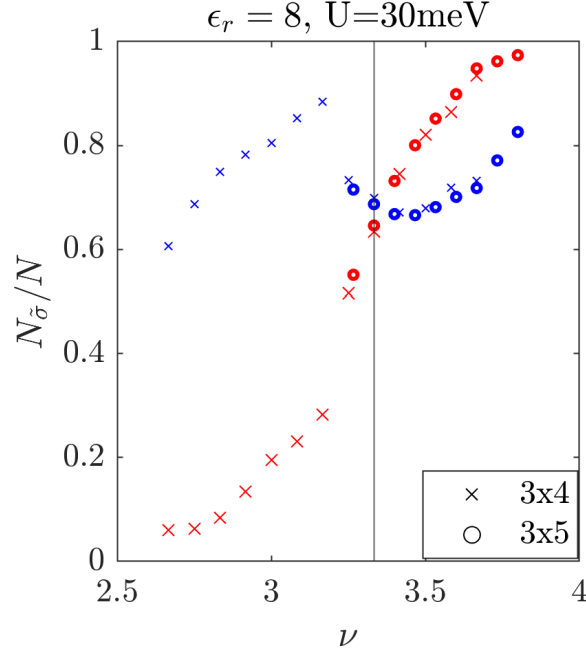


FIG. S10. 2-band ED calculation of the Chern-sublattice polarization as a function of filling. The legend indicates the lattice geometry of the cluster. $N_{\tilde{\sigma}}$ is the expectation value of the number of particles in the Chern-sublattice band $\tilde{\sigma}$. The vertical line corresponds to $\nu = 3 + 1/3$. We fix $\theta = 1.8^\circ$ and $U = 30$ meV. Red corresponds to the A sublattice, and blue corresponds to the B sublattice.

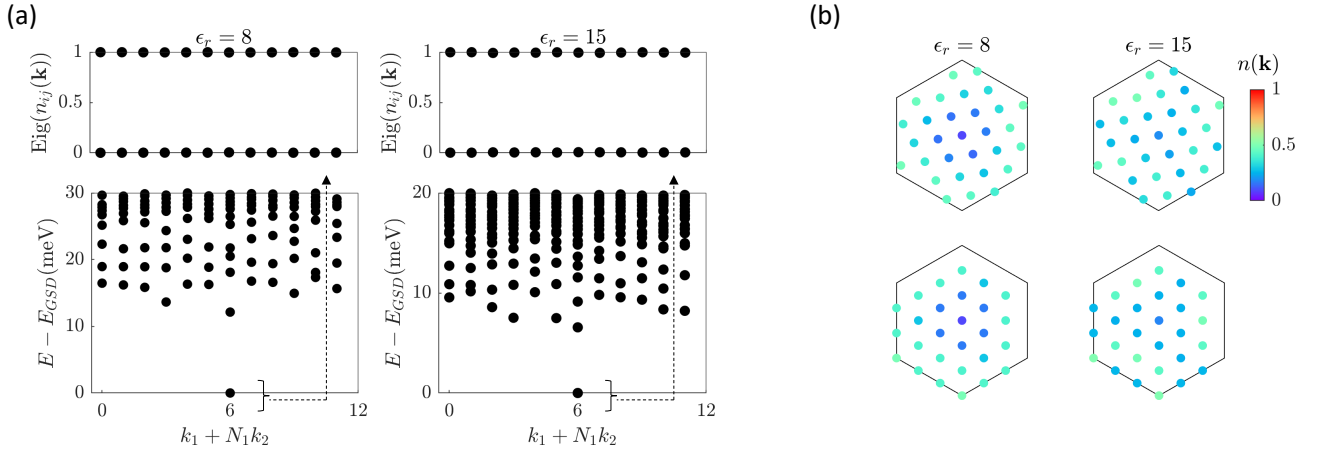


FIG. S11. (a) 2-band ED calculations at $\nu = 3$ with $\theta = 1.8^\circ$ and $U = 0$. Bottom panels show the momentum-resolved many-body spectrum. Top panels show the eigenvalues of the occupation matrix $n_{ij}(\mathbf{k})$ of the ground state. (b) Occupation number $n(\mathbf{k})$ of the many-body ground state obtained from 1-band ED performed at $\nu = 3 + 1/3$ with $\theta = 1.8^\circ$ and $U = 0$. We average over the three quasi-degenerate ground states. The top row is for the 30-site cluster, while the bottom row is for the tilted 27-site cluster.

4. Multi-band calculations of FCIs

In this subsection, we discuss multi-band ED calculations of FCIs in the fully flavor polarized sector at $\nu = 3 + \frac{1}{3}$. Owing to the $U(2)_K \times U(2)_{\bar{K}}$ symmetry of the Hamiltonian, we can focus our attention on the two bands within the single partially-occupied flavor. The main limitation of ED stems from the exponential growth of the many-body Hilbert space. While performing a 1-band calculation within the $\nu = +3$ HF conduction band significantly reduces the computational cost, this restriction ignores band mixing effects with the other band [88–92], which are potentially

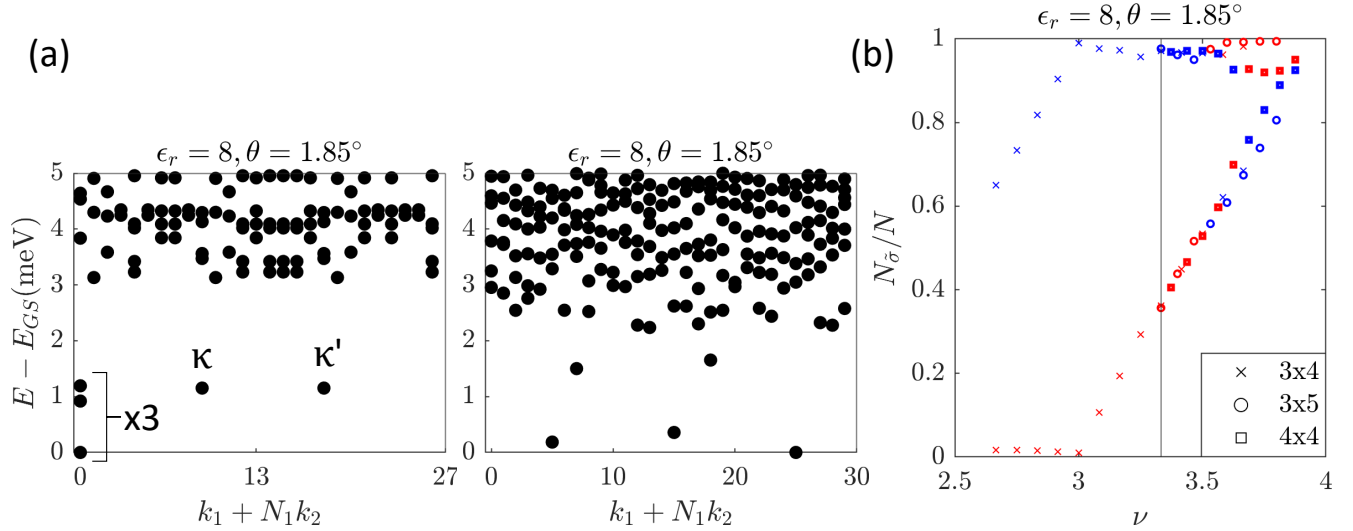


FIG. S12. **(a)** 1-band ED calculations on the tilted 27-site (left) and the 5×6 (right) cluster at $\nu = 3 + 1/3$. **(b)** 2-band ED calculation of the Chern-sublattice polarization as a function of filling. Different symbols (see legend) refer to various lattice geometries with corresponding system sizes $N = 12, 15, 16$. $N_{\bar{\sigma}}$ is the expectation value of the particle occupation in the Chern-sublattice basis. Red (blue) corresponds to the A (B) basis. The vertical line indicates $\nu = 3 + 1/3$. All calculations are performed at $\theta = 1.85^\circ$, $\epsilon_r = 8$, and with MDT.

important especially since the two non-interacting bands are not isolated.

One solution is to simply perform full 2-band calculations, but this severely limits the system sizes N that can be accessed. For example, the Hilbert space dimensions per momentum sector for $N = 15, 18, 21$ are $2 \times 10^6, 7 \times 10^7, 3 \times 10^9$. While $N = 18$ is in principle possible, it is out of reach of our current computational resources.

Another solution is to introduce a ‘bandmax’ constraint [91–93] that systematically interpolates between 1-band and 2-band calculations, and allows for larger N . We consider working in the $\nu = +3$ HF basis of the 2-band space. At $\nu = +3$, HF calculations yield a conduction band (which we refer to as A since it has high polarization on the A sublattice-Chern band) separated by a HF gap to the valence band (which we refer to as B). The HF and 2-band ED calculations show that the ground state at $\nu = 3 + 1/3$ continues to have near-complete occupancy of the B band. Hence for multi-band ED calculations at $\nu = 3 + 1/3$, we can constrain the many-body Hilbert space to include Fock states that include at most N_{\max} holes in the B band. $N_{\max} = 0$ corresponds to the 1-band calculation, while $N_{\max} = N$ corresponds to the full 2-band calculation. Based on the HF and 2-band ED results, we anticipate a rapid convergence with N_{\max} , so that we can effectively understand the low-energy 2-band physics at relatively small N_{\max} . For $N = 18$, an $N_{\max} = 4$ calculation at $\nu = 3 + 1/3$ has a Hilbert space dimension of 1×10^7 per momentum sector, which is within reach of our computational resources.

In Fig. S13, we present many-body spectra from 2-band ED calculations with bandmax restriction on a tilted $N = 18$ lattice for $\theta = 1.76^\circ$, $\epsilon_r = 8$ and $U = 0$ meV, as a function of flux-threading along the two handles of the torus. For $N_{\max} = 0$, i.e. a 1-band calculation, the system exhibits a three-fold quasi-degenerate ground state with the correct FCI momenta [65], and maintains a finite gap to the higher states under flux-threading. As N_{\max} is increased, the higher states drop in energy. However, the spectra are already well-converged by $N_{\max} = 2$. In particular, the three quasi-degenerate ground states remain well separated from the higher excitations, implying that the FCI survives in the 2-band limit. We caution that since the system size N is still quite small, it is not possible to reliably extract quantitative phase diagrams for the FCI, but the calculations here demonstrate that FCIs can exist even when accounting for the full multi-band freedom of the central bands.

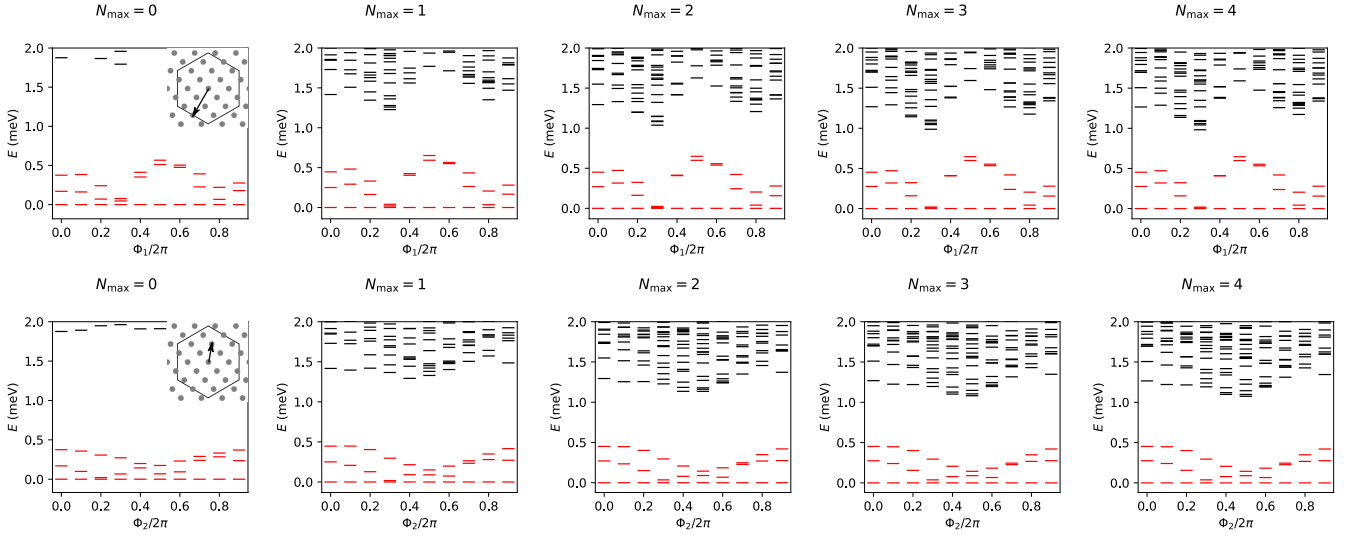


FIG. S13. 2-band $\nu = 3 + \frac{1}{3}$ ED calculations with bandmax restriction on the tilted 18-site lattice for $\theta = 1.76^\circ$, $\epsilon_r = 8$ and $U = 0$ meV. The horizontal axis of each panel refers to the flux threaded along one handle of the torus. The columns show the many-body spectrum for different values of N_{\max} , which denotes the maximum number of holes allowed in the lower HF band. The two rows correspond to threading flux along the two directions of the torus (see insets of the leftmost column for an illustration of the momentum mesh and the flux-threading direction). For the FCI momenta, we compute the two lowest states, while we only compute the lowest state for the non-FCI momenta. The lowest state in each FCI momenta is plotted in red. The many-body energies for each calculation are plotted relative to the lowest energy state across all momentum sectors.